Supplementary Information

Three-Dimensional Diffractive Acoustic Tomography

Luca Menozzi [a*], Tri Vu [a*], Aidan J Canning [a*], Harshal Rawtani [b], Carlos Taboada [a,c], Marie Elise Abi Antoun [d], Chenshuo Ma [a], Jesse Delia [e], Van Tu Nguyen [a], Soon-Woo Cho [a], Jianing Chen [a], Theresa Charity [f,g], Yirui Xu [a], Phuong Tran [a,h], Jun Xia [i], Gregory M. Palmer[f,g], Tuan Vo-Dinh [a,j,†], Liping Feng [b,†], Junjie Yao [a,k,†]

[a] *Department of Biomedical Engineering, Duke University, Durham, North Carolina, USA*

[b] *Duke University School of Medicine, Durham, North Carolina, USA*

[c] *Department of Biological Sciences, Vanderbilt University, Nashville, Tennessee, USA*

[d] *Tufts Medical Center, Boston, Massachusetts, USA*

[e] *American Museum of Natural History, New York City, New York, USA*

[f] *Department of Radiation Oncology, Duke University School of Medicine, Durham, NC 27710, USA*

[g] *Department of Surgery, Duke University School of Medicine, Durham, NC 27710, USA*

[h] *Department of Biomedical Engineering, North Carolina State University, Raleigh, North Carolina, USA*

[i] *Department of Biomedical Engineering, University at Buffalo, Buffalo, New York, USA*

[j] *Department of Chemistry, Duke University, Durham, NC 27708, USA*

[k] *Department of Neurology, Duke University of School of Medicine, Durham, NC 27710, USA*

**These authors contributed equally*

† Corresponding authors

Supplementary Note 1: 3D-DAT improves elevational resolution by single-slit diffraction

The Fraunhofer approximation gives the far-field pressure distribution of an acoustic wave passing through an aperture as the Fourier transform of the aperture geometry function. In the case of 3D-DAT, the single-slit aperture geometry A can be defined as a two-dimensional rectangular function along the lateral (x_1) and elevational axes (y_1) of the linear-array transducer:

$$A(x_1, y_1) = \mathrm{rect}\left(\frac{x_1}{H}\right)\mathrm{rect}\left(\frac{y_1}{W}\right). \quad (1)$$

Here, H and W are the height and the width of the single-slit, respectively. Given that the single-slit is effectively infinite in height and its diffractive effect is negligible (i.e., H is much larger than the acoustic wavelength), we have $\mathrm{rect}\left(\frac{x_1}{H}\right) \approx 1$, and thus our aperture function becomes dependent only on the single-slit width and elevational position,

$$A(x_1, y_1) \approx \mathrm{rect}\left(\frac{y_1}{W}\right). \quad (2)$$

By the Fraunhofer approximation, we have the acoustic pressure p at axial distance z and lateral and elevational offsets x_0 and y_0 as the 2D Fourier transform of the aperture function evaluated at the spatial frequencies $k_x = -\frac{kx_0}{z}$ and $k_y = -\frac{ky_0}{z}$, where $k = \frac{2\pi}{\lambda}$, and λ is the acoustic wavelength [1] (see **Supplementary Fig. 2a**):

$$p(x_0, y_0, z) \approx \frac{j\omega\rho_0 v_0}{2\pi R} e^{-jk\left[z + \frac{{x_0}^2 + {y_0}^2}{2z}\right]} \mathcal{F}\{A(x_1, y_1)\}. \quad (3)$$

Here, R is the distance from the origin of the transducer plane to the observation point (x_0, y_0, z), ω is angular frequency, ρ_0 is the equilibrium density of the medium, and v_0 is the sound velocity amplitude. We can note that only the Fourier transform of the aperture geometry term has a real effect on the relative pressure field profile at the x/y location of the observation point. We can reduce this term as

$$\mathcal{F}\{A(y_1)\} = W\frac{\sin(Wk_y/2)}{Wk_y/2} = W\mathrm{sinc}\left(\frac{Wy_0}{\lambda z}\right). \quad (4)$$

We can now define the directivity function of the pressure distribution, $D(\theta)$, where we approximate that in the far-field $\sin\theta \approx \frac{y_0}{z}$ $(when\ y_0 \ll z)$, as

$$D(\theta) = \mathrm{sinc}\left(\frac{W\sin}{\lambda}\right). \tag{5}$$

Defining the acceptance angle of the single-slit aperture as the full width at half maximum (FWHM) of the main lobe of the directivity function, we get the relationship

$$\theta_{FWHM} = 2\sin^{-1}\left(\frac{0.6\lambda}{W}\right). \tag{6}$$

From Eq. (6), it is clear that a narrow single-slit, i.e., a small *W*, leads to a large acceptance angle by the slit. We can define the total effective aperture as the collection of synthetic transducer elements made by scanning the slit along the elevational axis. The total effective aperture width, T_A, that we can achieve depends on the acceptance angle of each synthetic element, which is defined above as θ_{FWHM}. We can define the maximum effective aperture as the largest elevational distance, for a given axial distance, between two synthetic transducer elements at which their acceptance aperture intersects (see **Supplementary Fig. 2b**). Here, as the first-order approximation, we simply treat the acceptance aperture as a step function. Then the total aperture is calculated as

$$T_A \approx \frac{2z}{\tan\left(\frac{\pi-\theta_{FWHM}}{2}\right)}. \tag{7}$$

Given that the elevational resolution *ER* of the array transducer is inversely proportional to its total elevational aperture [2],

$$ER = \frac{\lambda z}{T_A}, \tag{8}$$

we can therefore attain

$$ER \approx \frac{\lambda}{2}\tan\left(\frac{\pi-\theta_{FWHM}}{2}\right), \tag{9}$$

which can be simplified to

$$ER = \frac{5}{6}\sqrt{W^2 - 0.36\lambda^2}. \tag{10}$$

Firstly, given that W is much larger than λ, Eq. (10) yields an approximately linear relationship between the slit width W and the elevational resolution ER for the slit-width-dominated regime, which is consistent with our experimental findings. Secondly, this result indicates that for 3D-DAT using a higher frequency transducer (i.e., shorter wavelength), the slit width must decrease accordingly to maintain the same total effective aperture width and the elevational resolution. Thirdly, it is interesting to note that, assuming a sufficiently large scan range, the elevational resolution for 3D-DAT is independent of the depth (*i.e.*, z axis), which is different from traditional PA/US imaging that relies on fixed elevational focusing. This is an important advantage of 3D-DAT over traditional PA/US imaging, which allows for a more consistent elevational resolution along the depth, as shown in **Figs. 3g-h**.

Supplementary Note 2: Characterization of FFL reconstruction and investigation of synthetic aperture width.

We compared the computational efficiency of our FFL reconstruction algorithm with the traditional delay-and-sum (DAS) reconstruction method (**Supplementary Fig. 6a**). Both reconstruction methods were written and executed in MATLAB, using a computer with 256 GB of random-access memory (RAM), an AMD Ryzen Threadripper 3970X central processing unit (CPU) (32 cores, 64 threads), and an NVIDIA RTX A6000 graphics processing unit (GPU) with 48 GB of GDDR6 VRAM and 10,752 CUDA cores.

In the traditional DAS method, a delay matrix was first calculated based on the distance between each transducer element and the reconstruction voxel. The dimensions of this delay matrix are $[n_x, n_y, n_z, n_e, n_{sa}]$, where n_x, n_y, and n_z are the dimensions of the reconstructed volume, n_e is the number of elements in the linear transducer array, and n_{sa} is the number of elements of the synthetic aperture (i.e., the scanning positions along the elevational axis). For a reconstruction volume of 40 x 40 x 10 mm (or 24 million voxels), the traditional DAS method needs ~8.7 minutes in total: ~42 seconds to calculate the delay matrix, ~8 minutes to reconstruct the volume using a CPU.

Similarly, the computational process in FFL can be divided into two tasks: the construction of the sparse matrix, and the multiplication of the sparse matrix with the RF data. The sparse matrix is of size $m \times n$, where m is the number of voxels in the reconstruction volume (i.e., $m = n_x \cdot n_y \cdot n_z$) and n is the total number of signal samples from all transducer elements in the synthetic aperture (*i.e.*, $n = n_e \cdot n_{sa} \cdot n_s$, where n_s is the number of samples in a single A-line). The location of the nonzero values in the sparse matrix corresponds to a certain index in the RF data. The values in the sparse matrix are either 0 or 1 (>99% of the values are 0, making this a highly sparse matrix). In this method, the reconstruction is performed by multiplying the RF data with the precalculated sparse matrix. For 24 million voxels, FFL needs ~1.5 minutes to calculate the sparse matrix, ~1.5 minutes to reconstruct the volume using a CPU, and ~10 seconds to reconstruct the volume using a GPU, which is ~50 times faster than the traditional method. It is important to note that the delay matrix in the traditional method and the sparse matrix in FFL need to be calculated only once and can be reused in any subsequent reconstructions.

Using FFL with a slit width of 0.8 mm, we further investigated the dependence of 3D-DAT's elevational resolution and SNR on the synthetic aperture width n_{sa} (**Supplementary Fig. 6b-d**). DPAT and DUST images were reconstructed using a synthetic aperture width ranging from 0.1 mm to 12 mm (**Supplementary Fig. 6b**, **Supplementary Movie 11** and **Supplementary Movie 12**). For DPAT, the elevational resolution plateaued at a synthetic aperture width of ~6 mm, while DUST plateaued at ~3 mm (**Supplementary Fig. 6c**). This difference is because DUST benefits from the round-trip acoustic diffraction by the slit. We observed that SNR peaked with a synthetic aperture width of ~2.5 mm for both DPAT and DUST (**Supplementary Fig. 6d**), due to the joint effect of the wave diffraction and wave attenuation by the slit. Based on these results, we used a synthetic aperture of 6 mm (or $n_{sa} = 60$) for all *in-vivo* experiments in this work.

Supplementary Note 3: Validation of 3D-DAT by phantom imaging.

The performance of 3D-DAT was quantified experimentally by imaging phantom targets. To validate the results obtained by our acoustic simulation, a crosshair phantom was imaged at various slit widths ranging from 0.08 mm to 2.0 mm (**Fig. 2c**, **d**, **Supplementary Movie 3**, and **Supplementary Movie 4**). The crosshair was fabricated from two black hairs (diameter: ~70−100 μm). The crosshair was sandwiched between two layers of agar, each layer being 5 mm thick. The agar was mixed with intralipid (1 mL intralipid per 35 mL solution) to incorporate optical scattering. The same imaging procedure at multiple slit widths was also performed with a star phantom (Thorlabs) to better investigate the angular dependence of resolution with various slit widths (**Supplementary Fig. 13**).

To quantify the depth of field and signal-to-noise ratio (SNR) of 3D-DAT as a function of depth, we imaged a staircase graphite phantom (**Fig. 2e**, **f**). The phantom was fabricated from four pieces of graphite (diameter: 300 μm) in agar mixed with intralipid. The four pieces of graphite were aligned with the lateral axis and arranged in a staircase fashion, ranging up to ~2 cm deep. The phantom was imaged with both DPAT and DUST using a slit width of 0.8 mm. DPAT characterization was performed at 1064 nm for all phantoms, except the blood oxygenation measurement (700 nm, 800 nm, and 870 nm).

To validate the functional imaging of DPAT, a blood tube phantom was fabricated (see **Figs. 2i-j** and **Supplementary Fig. 15**). Two silicon tubes (internal diameter: 300 μm) were sandwiched between two layers of agar (thickness: 5 mm) mixed with intralipid (1 mL intralipid per 35 mL solution). The outer tube was filled with oxygenated blood (100% oxygenation), made by mixing whole bovine blood with sodium bicarbonate (37 mg/mL). The inner tube was filled with deoxygenated blood (0% oxygenation), made by mixing whole bovine blood with sodium hydrosulfite (2.5 mg/mL) [3, 4]. Both tubes were attached to a syringe pump to induce blood flow and prevent clots from forming in the tubes. Three wavelengths of 700 nm, 800 nm, and 870 nm were used to image the phantom with DPAT.

Supplementary Note 4. Image metric definitions.

For all image quantifications used in these studies, we define signal-to-noise ratio (SNR) and contrast-to-noise ratio (CNR) as the following:

$$SNR = 20 \log_{10} \left(\frac{\mu_t}{\sigma_b} \right) \tag{11}$$

$$CNR = 20 \log_{10} \left(\frac{|\mu_t - \mu_b|}{\sigma_b} \right) \tag{12}$$

Here, μ_t is the average signal of the target region, σ_b is the standard deviation of the background region, and μ_b is the average signal of the background region. All target regions and background regions used for SNR and CNR calculations are marked in the respective images.

Supplementary Note 5: Estimation of oxygen saturation of hemoglobin (sO_2).

Estimation of sO_2 in the pregnant mouse study was performed by spectral decomposition of three excitation wavelengths: 700 nm, 800 nm, and 870 nm. By imaging at three separate wavelengths, we estimated the relative concentrations of oxyhemoglobin (HbO_2) and deoxyhemoglobin (HbR) by solving the following overdetermined system of linear equations using a least squares regression:

$$\begin{bmatrix} \varepsilon_{HbO_2}^{700} & \varepsilon_{HbR}^{700} \\ \varepsilon_{Hb\ _2}^{800} & \varepsilon_{HbR}^{800} \\ \varepsilon_{HbO_2}^{870} & \varepsilon_{HbR}^{870} \end{bmatrix} \begin{bmatrix} C_{HbO_2}(r) \\ C_{HbR}(r) \end{bmatrix} = \begin{bmatrix} \mu_{700}(r) \\ \mu_{800}(r) \\ \mu_{870}(r) \end{bmatrix}. \quad (13)$$

Here, $\varepsilon_{HbO_2}^{\lambda}$represents the molar extinction coefficient of HbO_2 at wavelength λ. $C_{Hb\ _2}(r)$ represents the concentration of HbO_2 at voxel r, and $\mu_{\lambda}(r)$ represents the reconstructed PA signal at voxel r with excitation wavelength λ. By performing a least squares regression using this overdetermined system to approximate $C_{HbO_2}(r)$ and $C_{HbR}(r)$,we can estimate the sO_2.

It is important to note that depth-dependent fluence at different wavelengths is not considered in the sO_2 estimation [5]. Therefore, the oxygenation estimation in deeper tissues becomes less accurate. Nevertheless, the three wavelengths were chosen to have relatively similar optical attenuation in tissue, mitigating the effect of wavelength-dependent fluence in our sO_2 estimations.

Supplementary Note 6: Animal preparation and imaging.

BALB/C mice (2-6 months old, Charles River labs) and glassfrogs of the species *Hyalinobatrachium fleischmanni* were used for our studies. Animals were housed on a 12 hour light 12 hour dark cycle, at a temperature of ~23°C, and humidity of 40-60%. A total of 13 mice were enrolled for our studies (1 mouse for validation imaging, 6 for the PFAS pregnancy study, and 6 for the GNS studies), and 1 glassfrog was enrolled for the BBS study. All animal procedures were approved by the Duke University Animal Care and Use Committee (protocol numbers A203-22-12 and A174-21-08), and were conducted in accordance with the United States Public Health Service's Policy on Humane Care and Use of Laboratory Animals.

Anesthesia was induced in mice using 5% isoflurane mixed with 30% O_2/70% N_2. After induction, the isoflurane was reduced to 1.5-2.0%. Hair was then removed from the area being imaged by first shaving the mouse with an electric razor, then applying a hair removal cream to the shaved region and wiping the remaining hairs away with a wet cotton swab. The mouse was then moved to the imaging platform which was filled with circulating warm water (maintained at 38ºC). The water cushion between the imaging platform and the linear-array transducer was filled with warm water (~40 ºC) to keep the area in contact with the mouse body warm. 3D-DAT was then performed, where the US and three PA wavelengths (532 nm, 1064 nm, and the OPO wavelength) were acquired concurrently at 10 Hz. Only one US plane wave and one laser pulse at each wavelength was transmitted at each elevational scanning position. The elevational scanning range was 3-4 cm, depending on the target area being imaged, with a step size of 0.1 mm. Thus, each scan was completed in 30-40 seconds. When more OPO wavelengths were needed, the transducer returned to its start position and the scan was repeated with the new wavelength (Supplementary Fig. 4).

Glassfrogs were anesthetized using 3-aminobenzoic acid ethyl ester (MS222, Sigma) 0.04%, buffered with 0.1% sodium bicarbonate (pH 7). This treatment is known to result in extensive blood perfusion [6]. Frogs were placed in a custom-made circular imaging chamber lined with an optically and acoustically transparent PVC membrane (thickness: 10 μm). The imaging platform was filled with water at room temperature (21 ºC). 3D-DAT

was then performed, where one US and three PA images (532 nm, 1064 nm, and 673 nm) were acquired at 10 Hz. The wavelengths were selected to target hemoglobin absorption peaks (532 and 1064 nm) and the Q-band of the biliverdin-binding serpins of the glassfrog *H. fleischmanni* (673 nm) [6, 7].

Supplementary Note 7. Statistical analysis.

We performed statistical comparisons for our tumor oxygenation study and our pregnancy study. In our tumor oxygenation study, the tumor region and the contralateral main blood vessel were manually segmented, and the average sO_2 value was calculated (n = 3 mice). We employed a two-sample t-test to determine with significant confidence ($p < 0.05$) that the oxygenation in the tumor differed from the oxygenation in the blood vessel. For our pregnancy study, both embryos and maternal vessels were manually segmented in the DPAT data and validated with the corresponding high-frequency US for all gestational days. The average sO_2 for maternal vessels regions and each individual embryo region was calculated, and the embryo sO_2 values were normalized to the corresponding maternal vessel sO_2 to attain the EV/MV ratio. For both control and PFAS exposed groups (n = 3 mice/group), all EV/MV ratios for each embryo and mouse were grouped based on the gestational ages shown in Fig. 5d. Two-sample t-tests were used to determine with significant confidence ($p < 0.05$) that EV/MV ratios of corresponding gestational ages differed between the control and PFAS-exposed groups. All statistical data are presented with standard deviation.

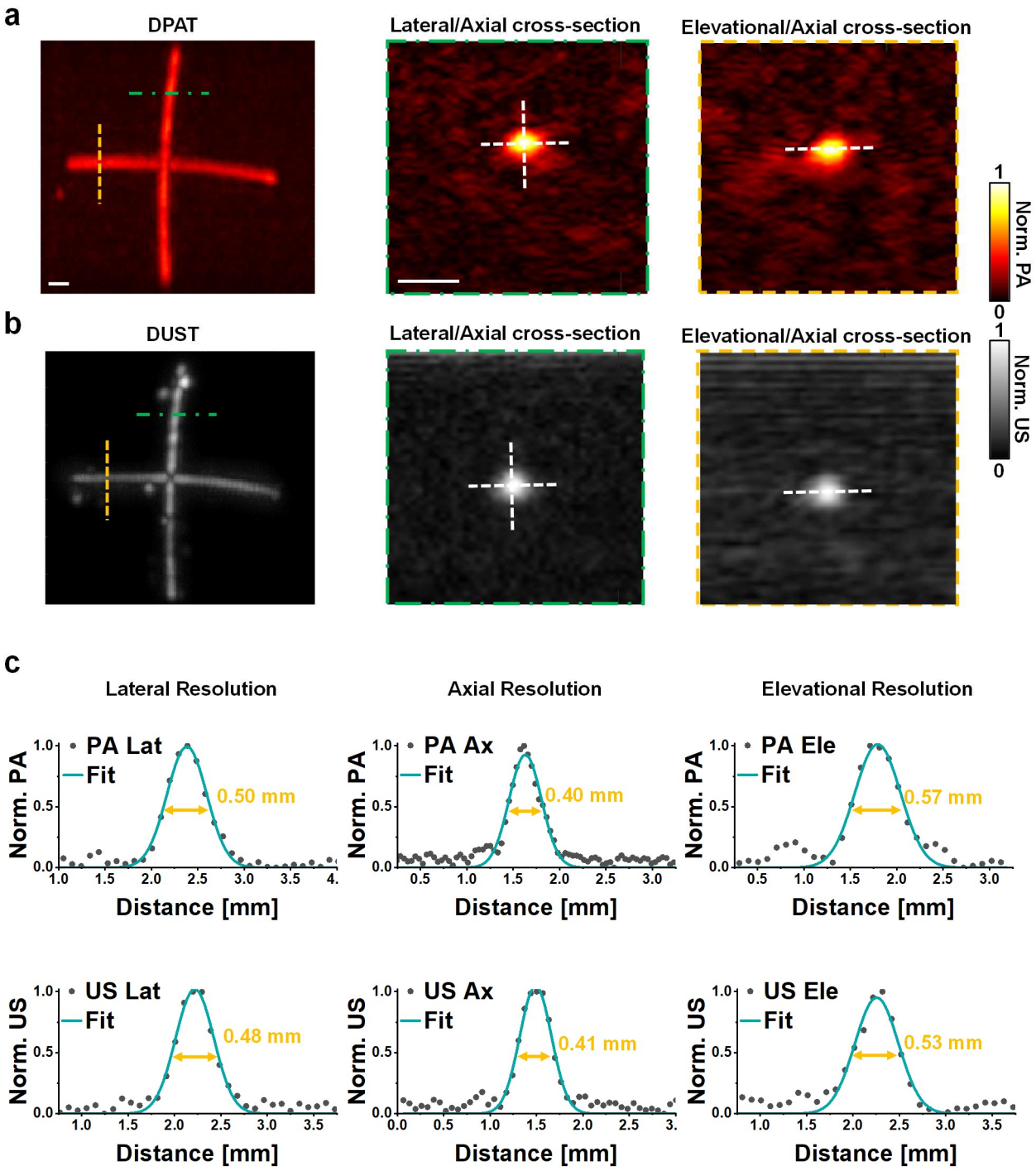

Supplementary Figure 1. 3D resolutions of 3D-DAT with a 0.8 mm slit width. (a) PA image of a cross-hair target. The dashed lines indicate where lateral/axial and elevational/axial cross sections were analyzed to quantify the resolutions. The hair diameter is about 0.1 mm. **(b)** Corresponding US image of the cross-hair target. The dashed lines indicate where lateral/axial and elevational/axial cross sections were

analyzed to quantify the resolutions. **(c)** PA (top) and US (bottom) image profiles. The full width at half maximum (FWHM) of each profile is quantified for each profile as the spatial resolution. Scale bars, 1 mm.

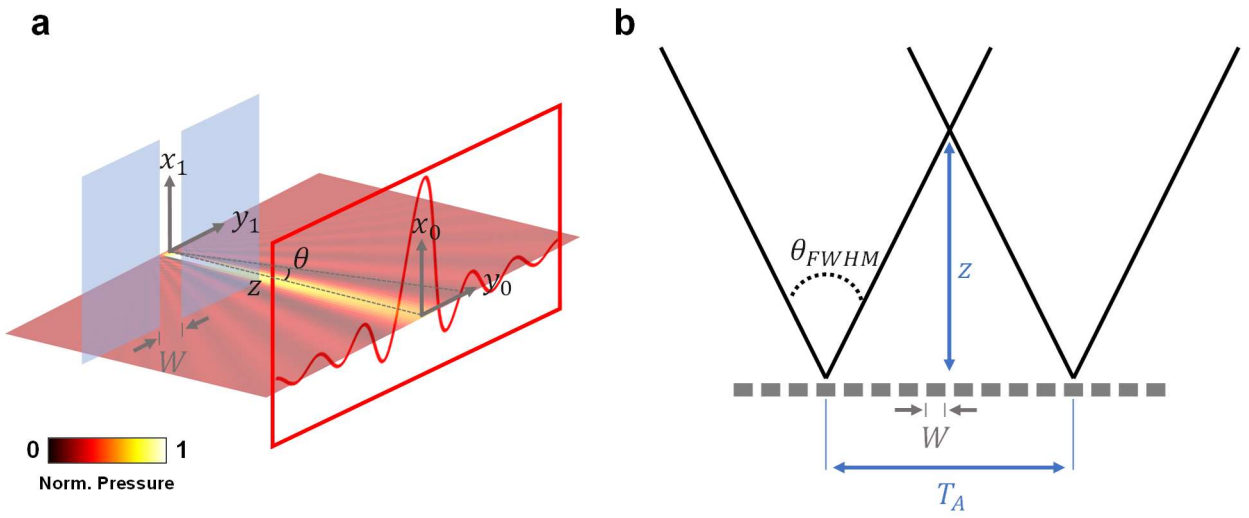

Supplementary Figure 2. Single-slit diffraction can improve elevational resolution. **(a)** Schematic of single-slit diffraction producing a sinc-shaped pressure field. Reducing the slit width *W* will increase the main lobe of the sinc waveform, thus increasing the diffraction angle and acceptance aperture. **(b)** Diagram of resolution enhancement due to increased angular sensitivities of individual synthetic elements. The maximum elevational aperture T_A depends on the receiving angle of each individual element. For a given depth z, we can consider the maximum aperture to be defined by two farthest elements whose receiving apertures can still intersect.

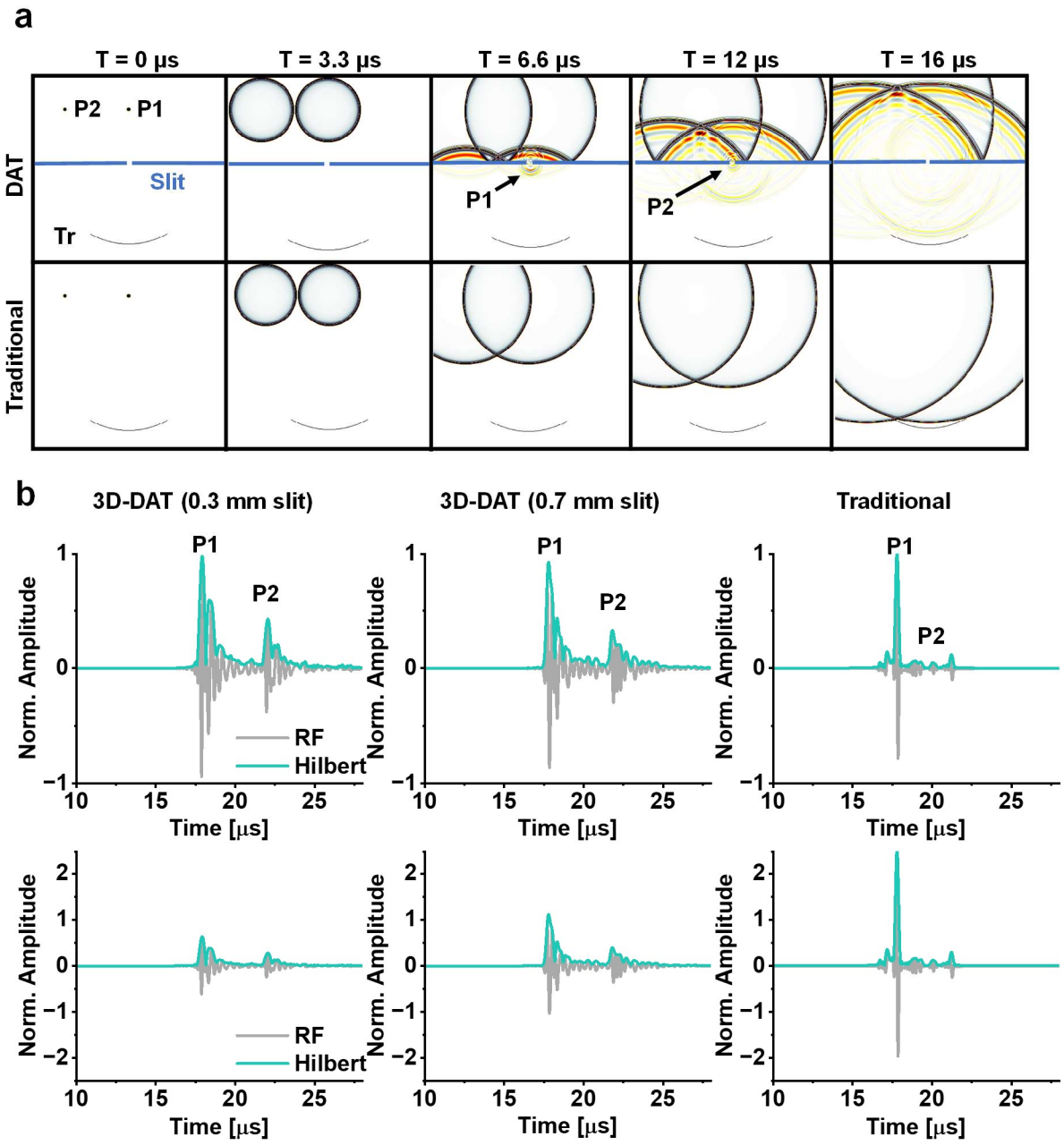

Supplementary Figure 3. k-Wave simulation of slit diffraction in 3D-DAT for on-axis and off-axis point targets. (a) Simulation of photoacoustic point sources P1 and P2. P1 is on the elevational axis of the linear-array transducer and P2 is off the elevational axis. The PA signals from P1 and P2 are propagating to the elevationally-focused linear transducer array with and without a slit present. With a slit present (i.e., 3D-DAT), all ultrasound waves that propagate through the slit, independent of the source location (both P1 and P2), are redirected by the slit at the focal position. This leads to coherent

integration of the diffractive waves at the transducer surface. Without the slit present (i.e., traditional PA imaging), only the ultrasound waves from P1 are received by the transducer in a coherent manner, while the waves from P2 are not received coherently. **(b)** Ultrasound signals detected by the transducer over the time course of the simulation for three different simulation settings. 0.3 mm slit, 0.7 mm slit, and no slit. The top row shows individually normalized signals, and the bottom row shows corresponding globally normalized signals. With the slit present, the P1 signals decrease but P2 signals increase, reflecting the broadening of the receiving aperture of the transducer. The ability to detect off-axis signals from P2 allows for the generation of a synthetic matrix aperture when scanning the transducer along the elevational axis.

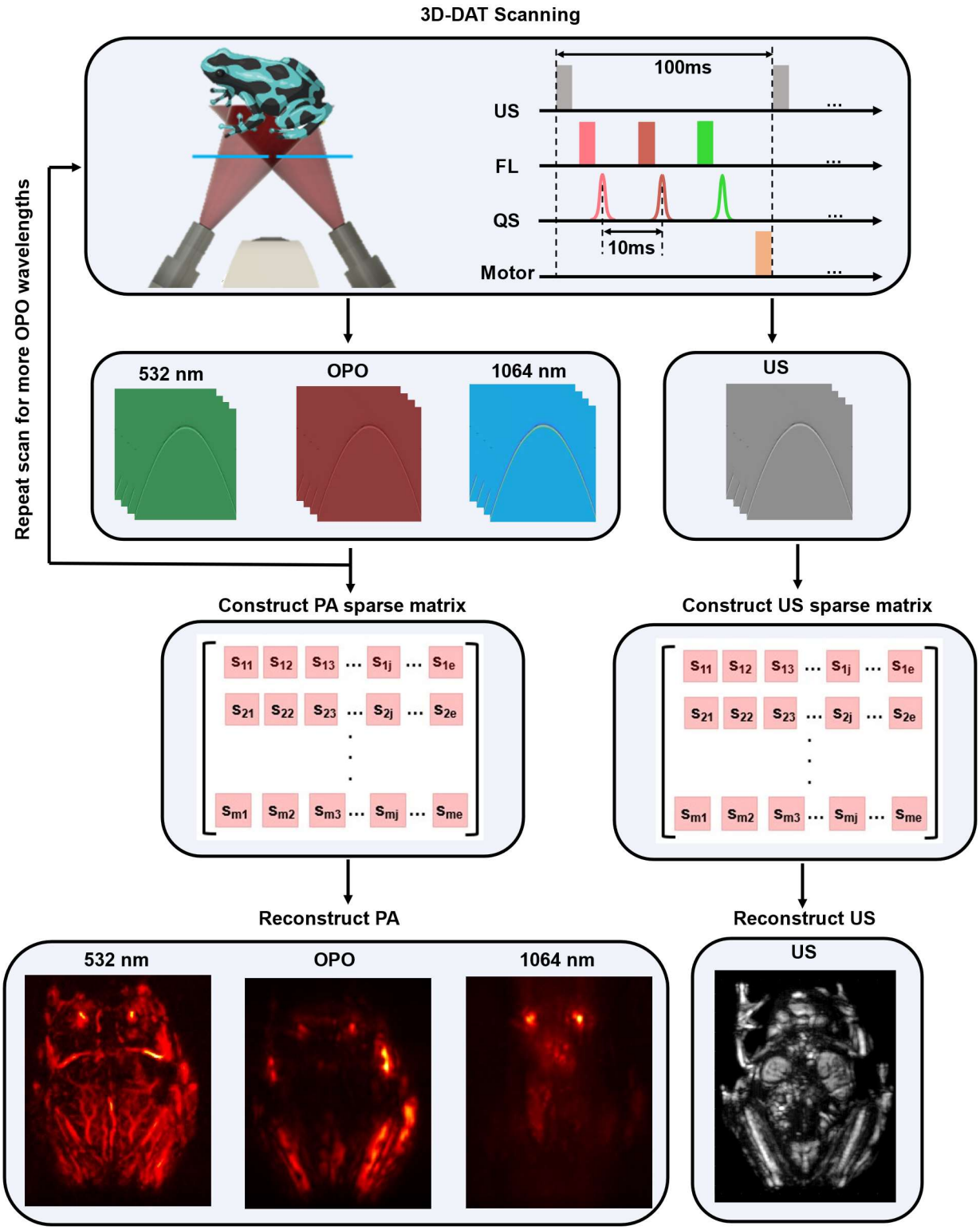

Supplementary Figure 4: Imaging and data processing pipeline of 3D-DAT. Ultrasound is first acquired by a zero-angle plane wave transmission. This is followed by an OPO laser pulse, then 1064 nm laser pulse, then 532 nm laser pulse. Each pulse is

separated by 10 ms, allowing sufficient time for the photoacoustic wave to be collected by the transducer without mixing. Following each data acquisition cycle, the transducer and slit are scanned one step along the elevational axis, and the process is repeated. Once the transducer and slit have been fully scanned across the sample, the data can be reconstructed via the sparse-matrix-multiplication-based FFL reconstruction. Created in BioRender. Menozzi, L. (2025) https://BioRender.com/l50m675.

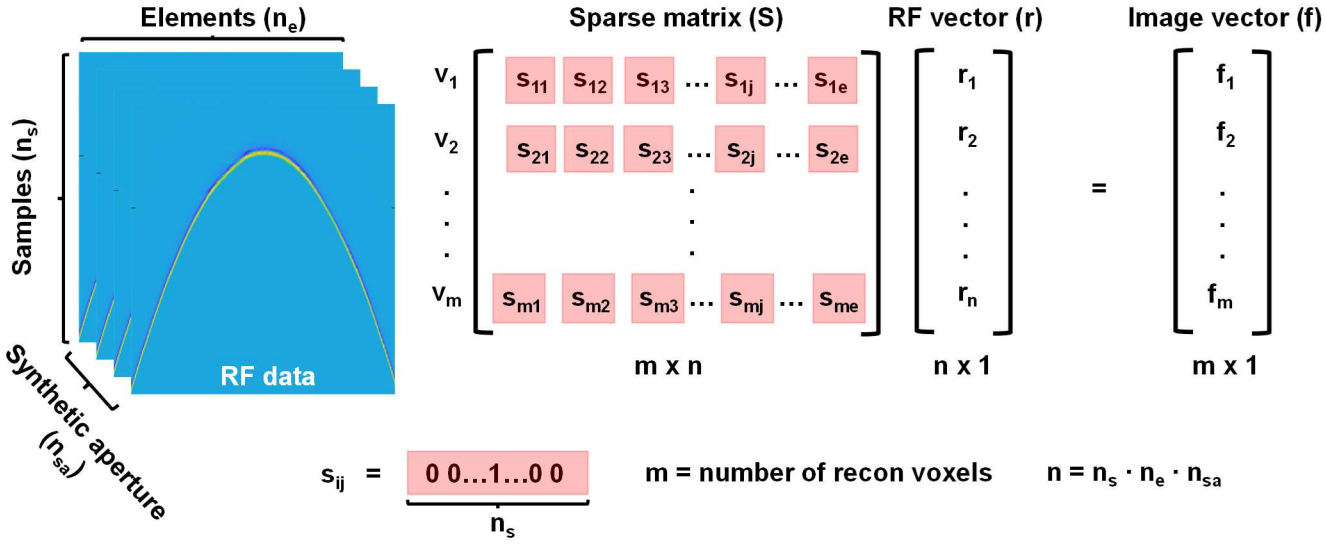

Supplementary Figure 5. FFL reconstruction algorithm. Example radio frequency (RF) data recorded by the linear transducer array in 3D-DAT, arranged as elements (n_e) by total samples per element (n_s) by synthetic aperture positions (n_{sa}, also the elevational scanning positions). The sparse matrix (S) is constructed by calculating the focal line path from each element to each reconstruction voxel and converting the distance to a time delay. S is m x n, where m is the total number of reconstruction voxels and n is the number of samples times the number of elements times the size of the synthetic aperture. Multiplying the flattened RF data by the sparse matrix yields the complete reconstruction vector, which is then reshaped into a 3D volume.

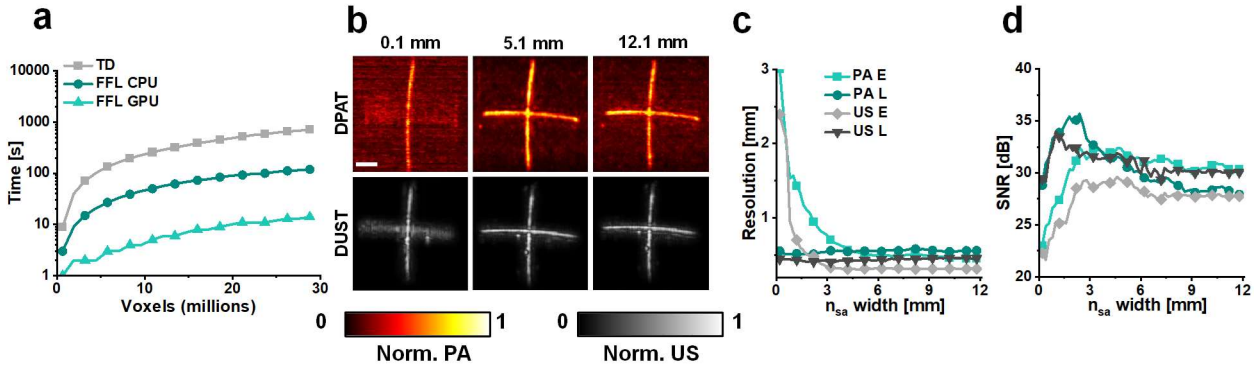

Supplementary Figure 6. Characterization of FFL reconstruction and investigation of synthetic aperture width. (a) Comparison of FFL reconstruction speed using CPU and GPU with delay matrix indexing. A synthetic aperture of 6 mm was used for FFL reconstructions, allowing for a large reduction in computation time with minimal change in image quality. **(b)** PA and US images of a cross-hair target reconstructed using different synthetic aperture widths. The slit width was 0.8 mm. **(c-d)** Resolution **(c)** and SNR **(d)** of DPAT and DUST as a function of synthetic aperture width.

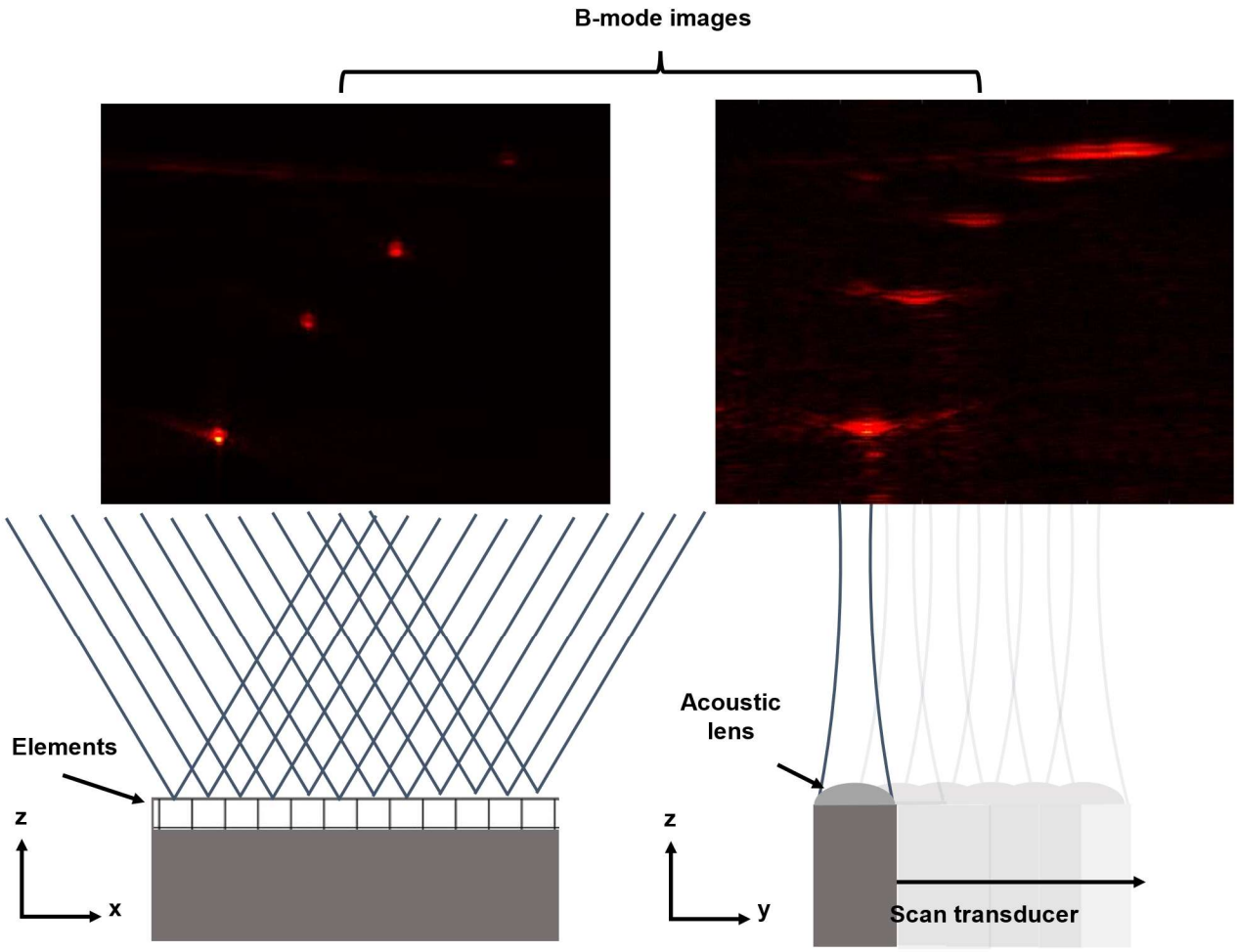

Supplementary Figure 7. 3D image formation in traditional PA imaging by scanning a linear-array transducer.

Left. Each cross-sectional image (lateral-axial image plane) with a linear-array is formed by beamforming reconstructions that utilize the wide acceptance angle of small elements and large lateral transducer aperture, with a high lateral resolution.

Right. By scanning the linear-array transducer, a synthetic aperture can be generated along the elevational axis. However, the fixed acoustic focus results in a large synthetic element size with small acceptance angles, resulting in a poor elevational resolution.

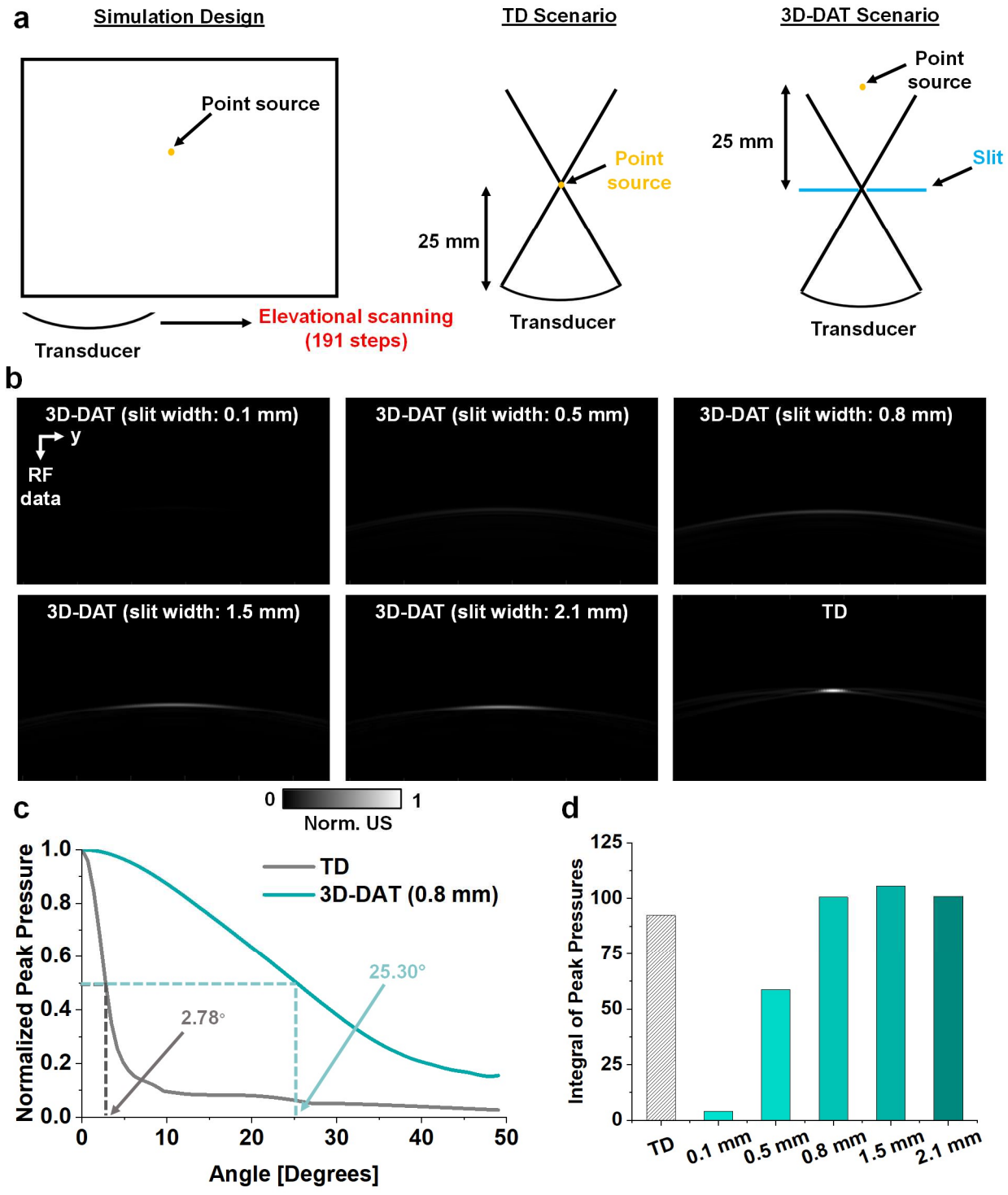

Supplementary Figure 8. k-Wave simulation of acoustic pressure and angular sensitivity in 3D-DAT. (a) Design of 2D k-Wave simulation, where a focused ultrasound transducer was scanned across a point source with a scanning step size of 0.2 mm, simulating the elevational scanning in 3D-DAT. The point source acted as the signal

pressure either in the PA or US imaging mode. Two types of scenarios were simulated, depicted on the right. In the traditional (TD) imaging scenario, the point source was placed at the focal position of the transducer with a focal length of 25 mm. In the 3D-DAT scenario, a slit was placed at the focal position of the transducer, and the point source was placed 25 mm from the slit. The point source was placed 25 mm away from the slit to avoid the effect of geometric spreading for the fair comparison between the TD imaging and 3D-DAT, since the slit aperture becomes the effective synthetic transducer for the 3D-DAT method. **(b)** Hilbert-transformed pressure data for five different slit widths in the 3D-DAT, as well as the corresponding TD imaging. For smaller slit widths, the reduced acoustic pressure is due to less acoustic energy passing through the slit, while the increased spread of the pressure is due to increased acceptance angle. (c) Angular sensitivity plot of traditional imaging and 3D-DAT. 3D-DAT shows nearly ten-fold increase in the acceptance angle at 0.8 mm slit width. (d) Integrated peak pressures over all angles for traditional imaging and 3D-DAT at varying slit widths, showing that 3D-DAT achieves comparable total detected pressure at the slit width of 0.8 mm and above.

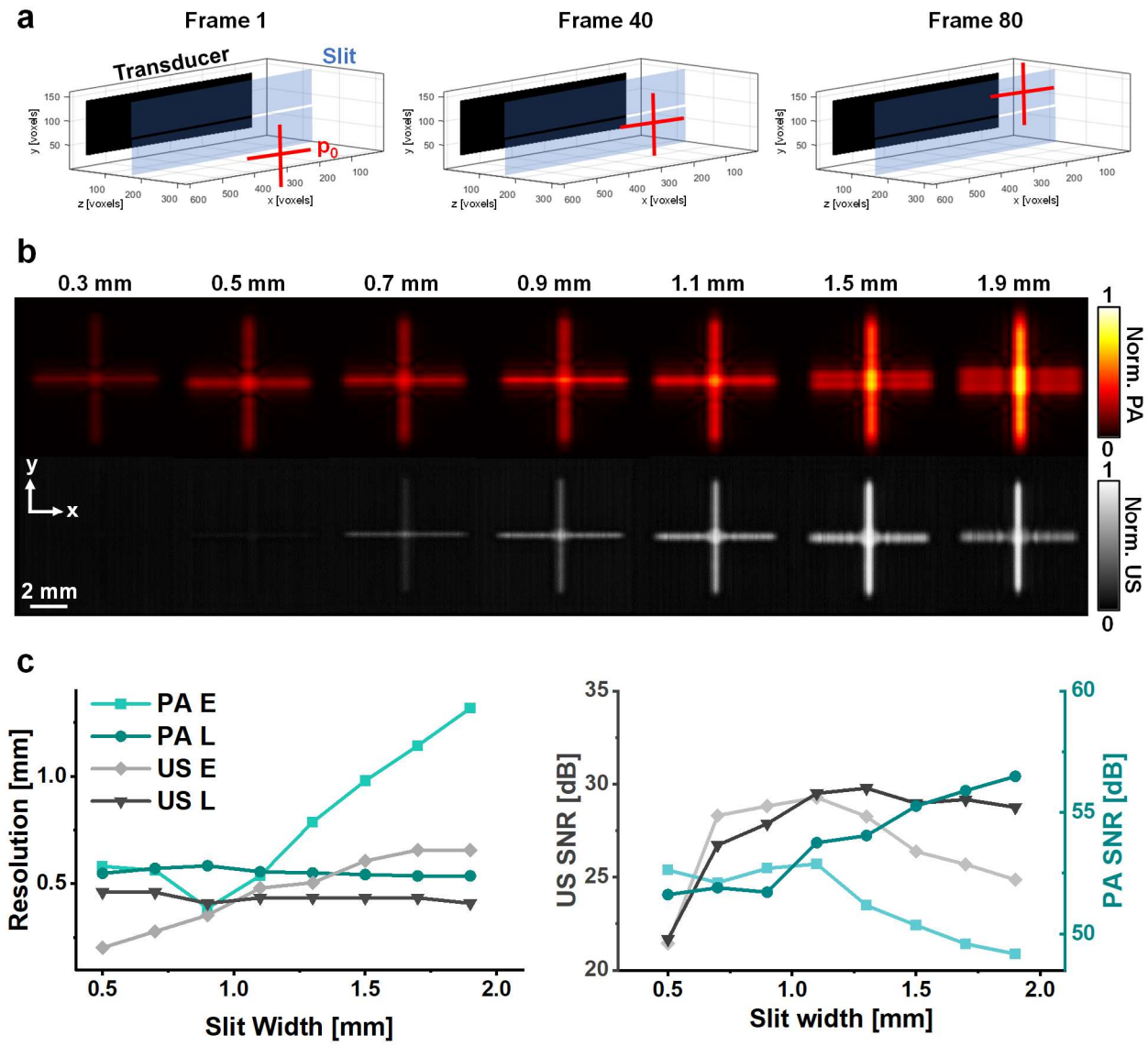

Supplementary Figure 9. 3D k-Wave simulations of 3D-DAT on a cross-hair phantom. (a) Geometry of the 3D k-Wave simulation. The linear-array transducer and slit remain stationary while the cross-hair is scanned along the y-axis (elevational) for each simulation. One 3D simulation is performed per cross-hair y-axis position. **(b)** Reconstructed DPAT and DUST images using different slit widths. **(c)** Plots of resolution and SNR as a function of slit width for both PA and US modes. E, elevational axis; L, lateral axis. A slit width of 0.8 mm provides the most balanced resolution enhancement and SNR improvement for the elevational axis.

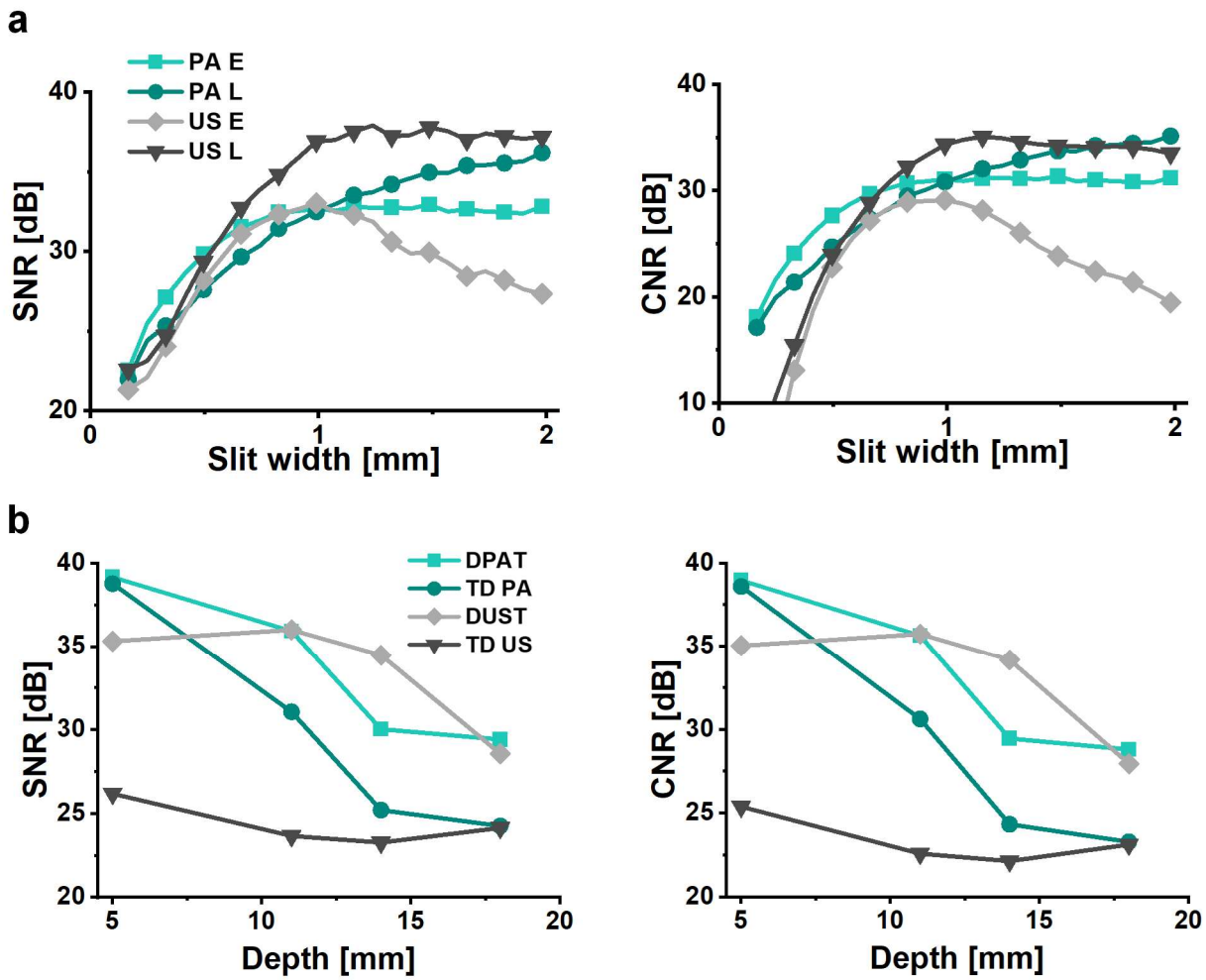

Supplementary Figure 10. Signal to noise ratio (SNR) and contrast to noise ratio (CNR) in 3D-DAT. (a) SNR and CNR as a function of slit width in 3D-DAT of a cross-hair phantom. **(b)** SNR and CNR at four depths of a graphite phantom. Trends in both SNR and CNR are similar. The same regions were used to compute the background signals and noise.

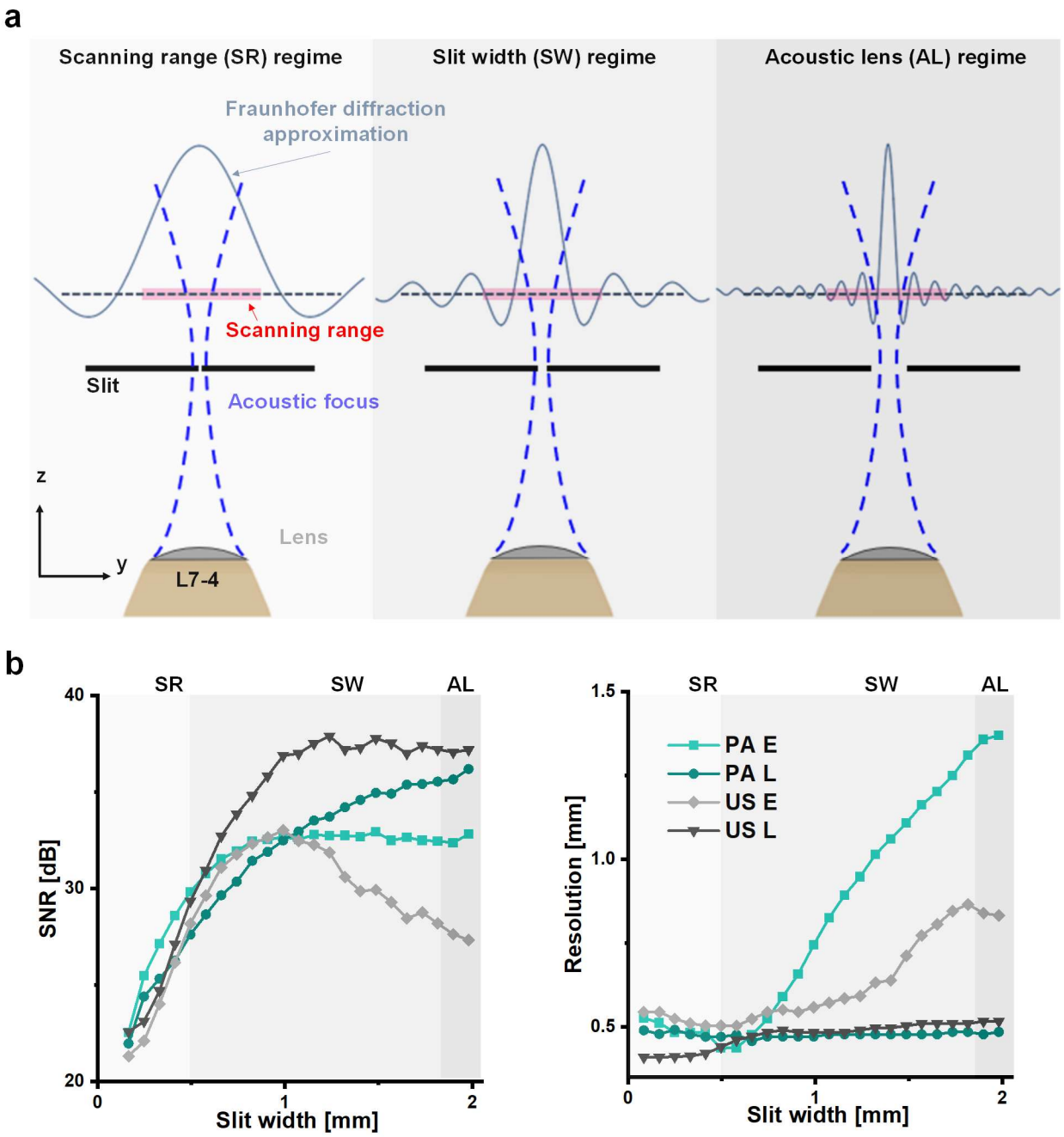

Supplementary Figure 11. Illustration of different elevational resolution regimes of 3D-DAT. (a) Three elevational resolution regimes of 3D-DAT, depending on the elevational scanning range, slit width, and elevational focusing of the transducer. The gray plots are the Fraunhofer approximations of far-field diffraction patterns, showing the width of the main diffraction lobe (directly corresponding to the transducer's angular sensitivity

along the elevational axis). **(b)** Elevational resolution regimes of 3D-DAT overlaid with the SNR and resolutions as a function of the slit width.

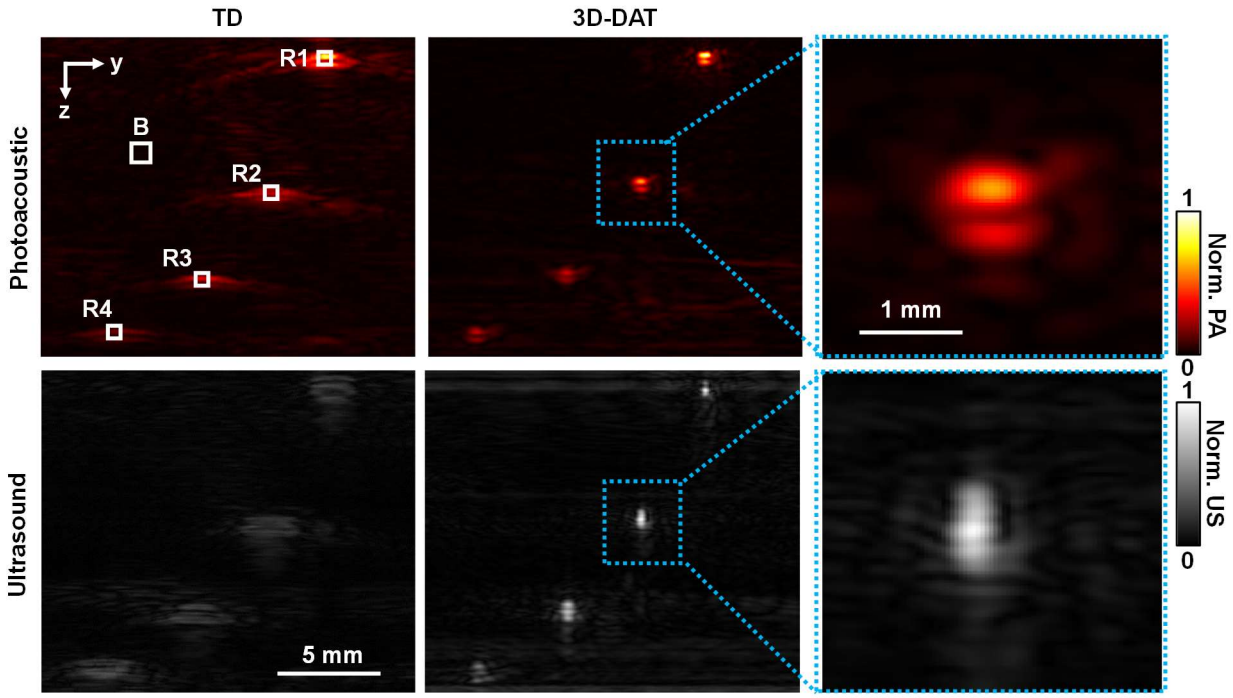

Supplementary Figure 12. Regions used for SNR and CNR calculations of the staircase graphite phantom. The complete photoacoustic (top) and ultrasound (bottom) cross-sectional images of the staircase graphite phantom in both traditional imaging and 3D-DAT methods. The four target regions (R) and the background region (B) from the elevational/axial cross-section used to compute SNR and CNR are marked. The same regions were used for both traditional imaging and 3D-DAT. For CNR calculations, B was used for calculating both the background standard deviation and the background mean.

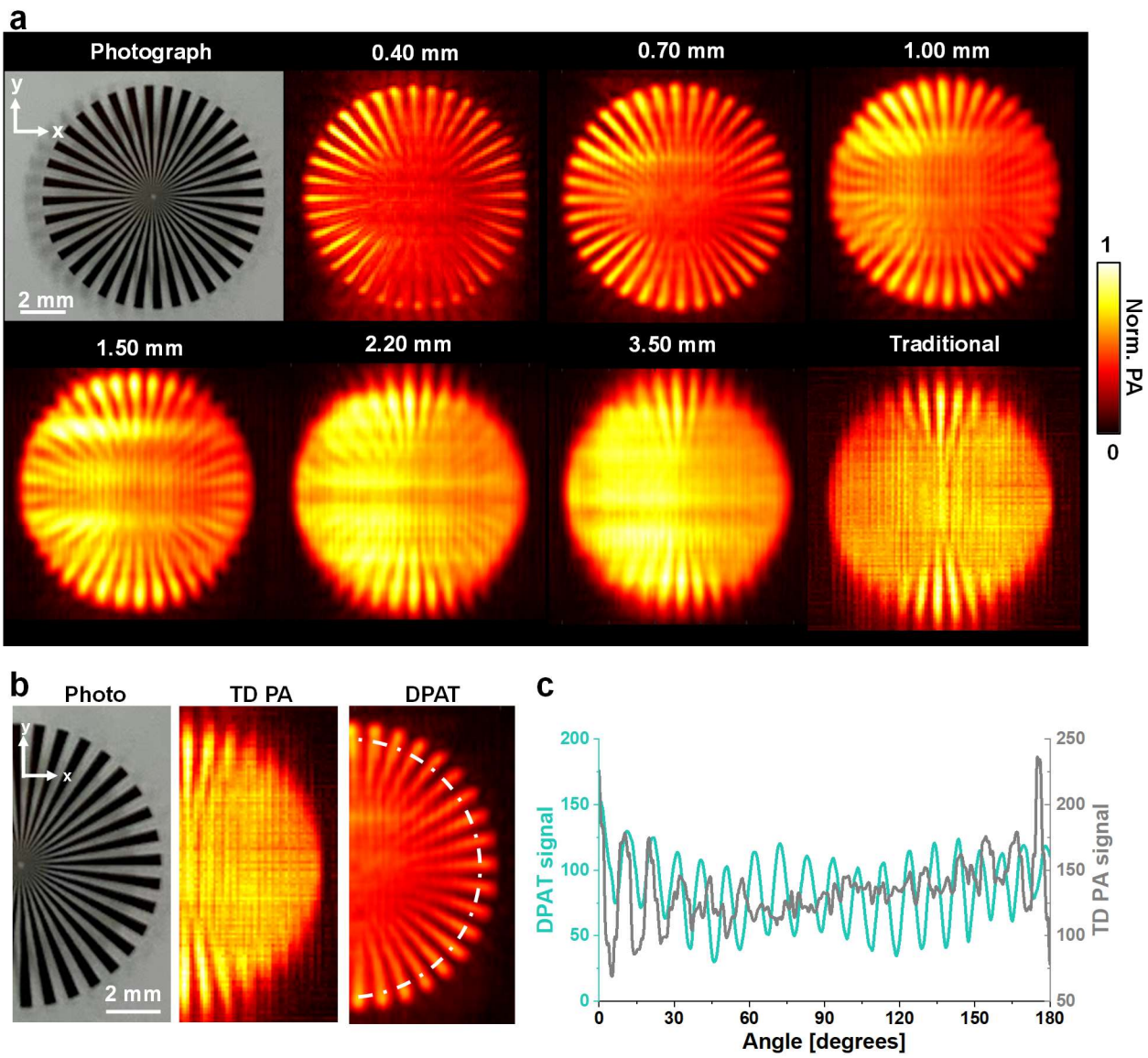

Supplementary Figure 13: Imaging a star phantom using DPAT. (a) DPAT and traditional PA images of a star phantom (Thorlabs) at various slit widths. The degradation in elevational resolution of DPAT with the increasing slit width is clear, while its lateral resolution remains independent of slit width. The traditional PA imaging has no slit present. **(b)** Traditional PA and DPAT images of a star phantom. **(c)** Profiles along white dashed line in **(b)** for traditional PA and DPAT images. In the DPAT image, the lines are clearly resolvable at all regions through the profile.

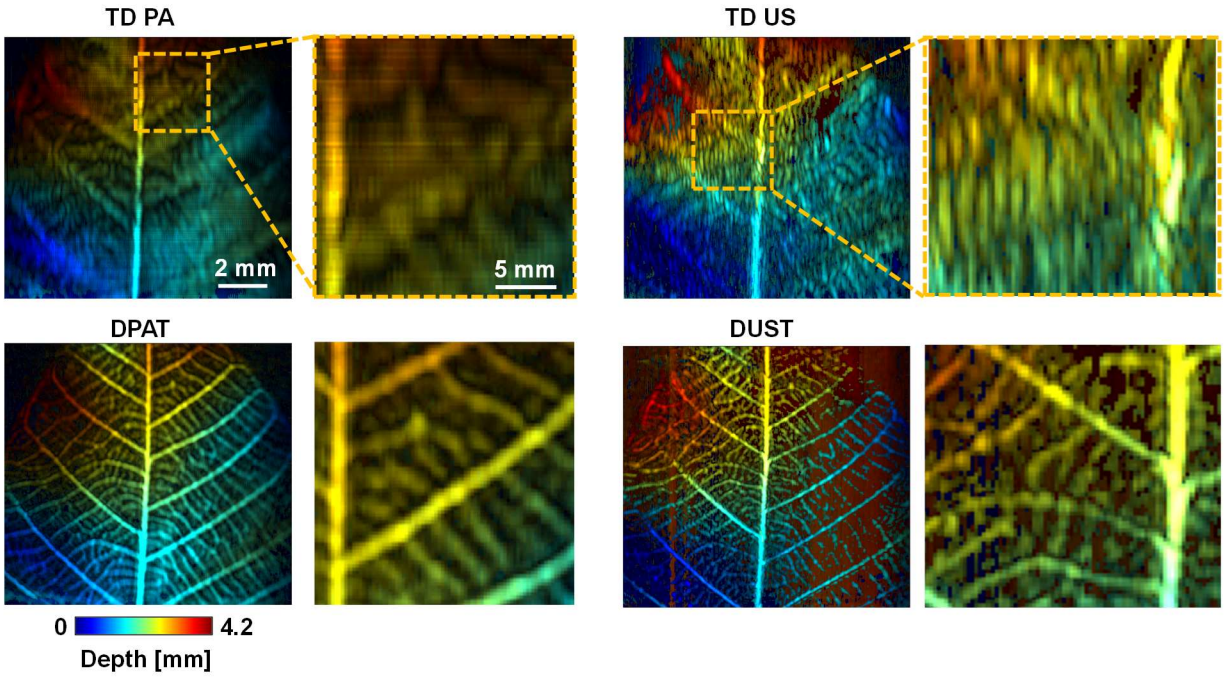

Supplementary Figure 14. Implementing 3D-DAT with a GE 9L-D transducer. Depth-encoded traditional PA/US and corresponding 3D-DAT images of a skeleton leaf target. The GE 9L-D transducer has a frequency range of approximately 3-8 MHz, yielding a similar central frequency as the L7-4 transducer of about 5.2 MHz. The array has 192 elements with a pitch of 0.23 mm, yielding a total lateral aperture of ~44 mm. Additionally, the individual element height is 6 mm, and the transducer is built with an acoustic lens focused at a distance of 40 mm.

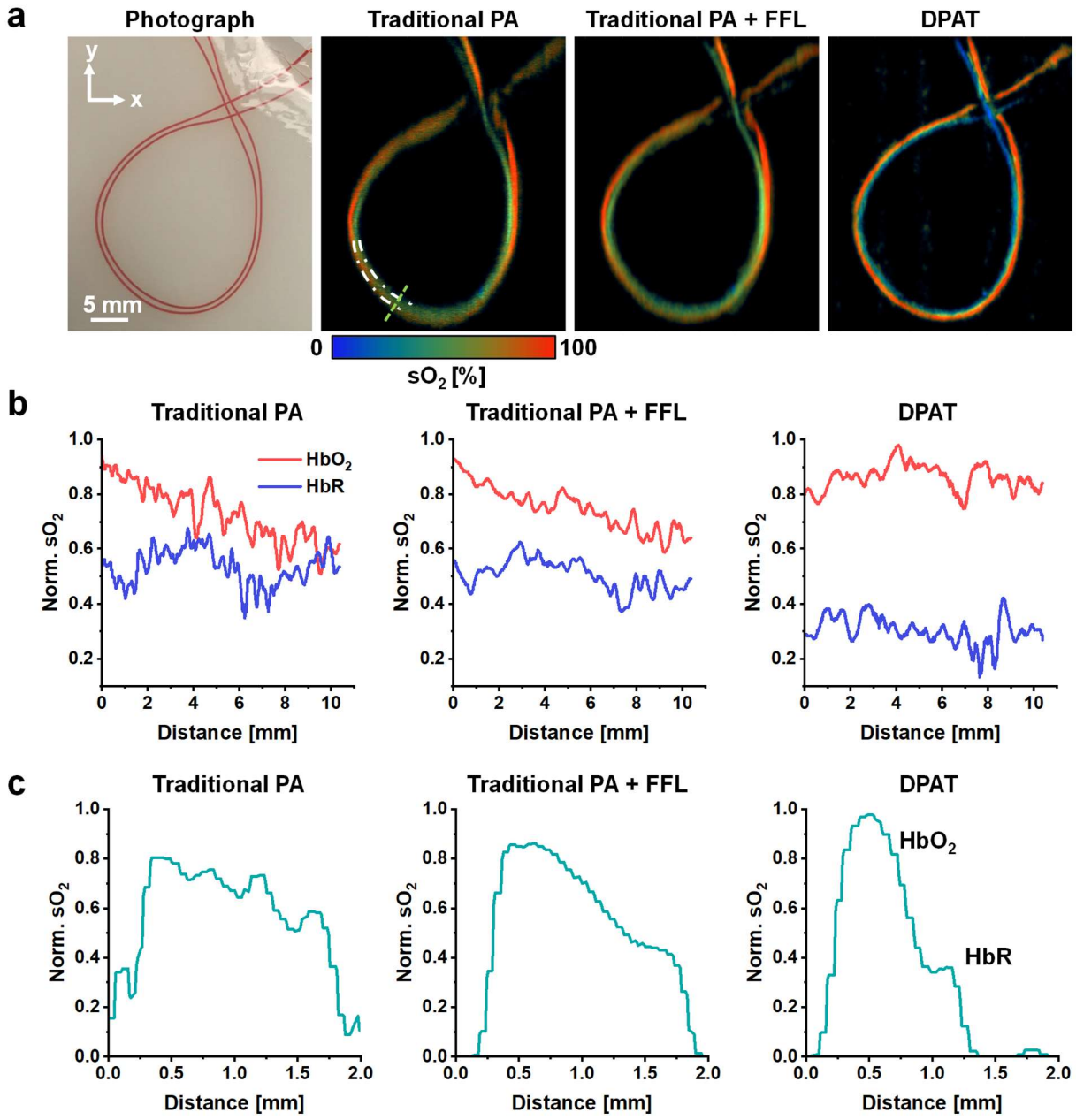

Supplementary Figure 15. Oxygenation measurement by DPAT on a blood tube phantom. (a) Photograph of the blood tube setup (oxygenated tube on the outside, deoxygenated tube on the inside). The oxygenation (sO_2) of the tubes were measured by using three different methods. Traditional PA (no slit) with direct delay and sum image reconstruction, traditional PA with fast focal line (FFL) reconstruction, and DPAT (0.8 mm slit width) with FFL reconstruction. **(b)** sO_2 profiles along the tubes as indicated by white dashed lines in **(a)**. In both traditional PA images, the oxygenation profiles merge as the

tubes align more with the lateral axis. In the DPAT image, the oxygenation profiles remain consistent, showing the importance of isotropic resolutions for accurate functional measurements. **(c)** sO_2 profiles across the tubes as shown by the green dashed line in **(a)**. In the DPAT image, the oxygenated and deoxygenated tubes are clearly distinguishable along the profile, while in both traditional PA images the two tubes become blurred together due to poor elevational resolution.

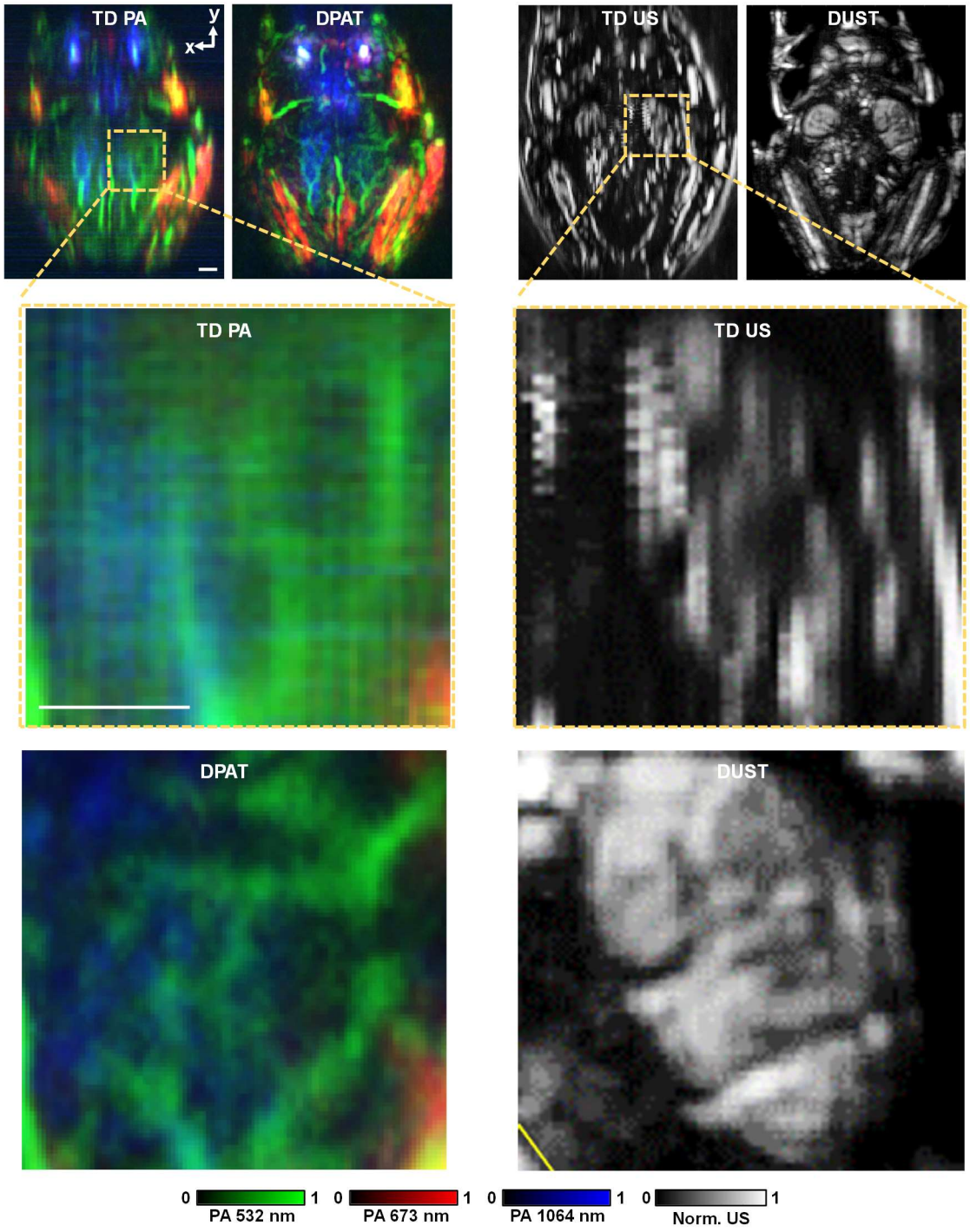

Supplementary Figure 16. 3D-DAT of a glassfrog *in-vivo.* Multiwavelength DPAT shows clear improvement in both resolution and sensitivity over traditional PA imaging in the close-up bladder images. DUST similarly shows clear improvements compared to traditional US image in the close-up lung images. Scale bars, 2 mm.

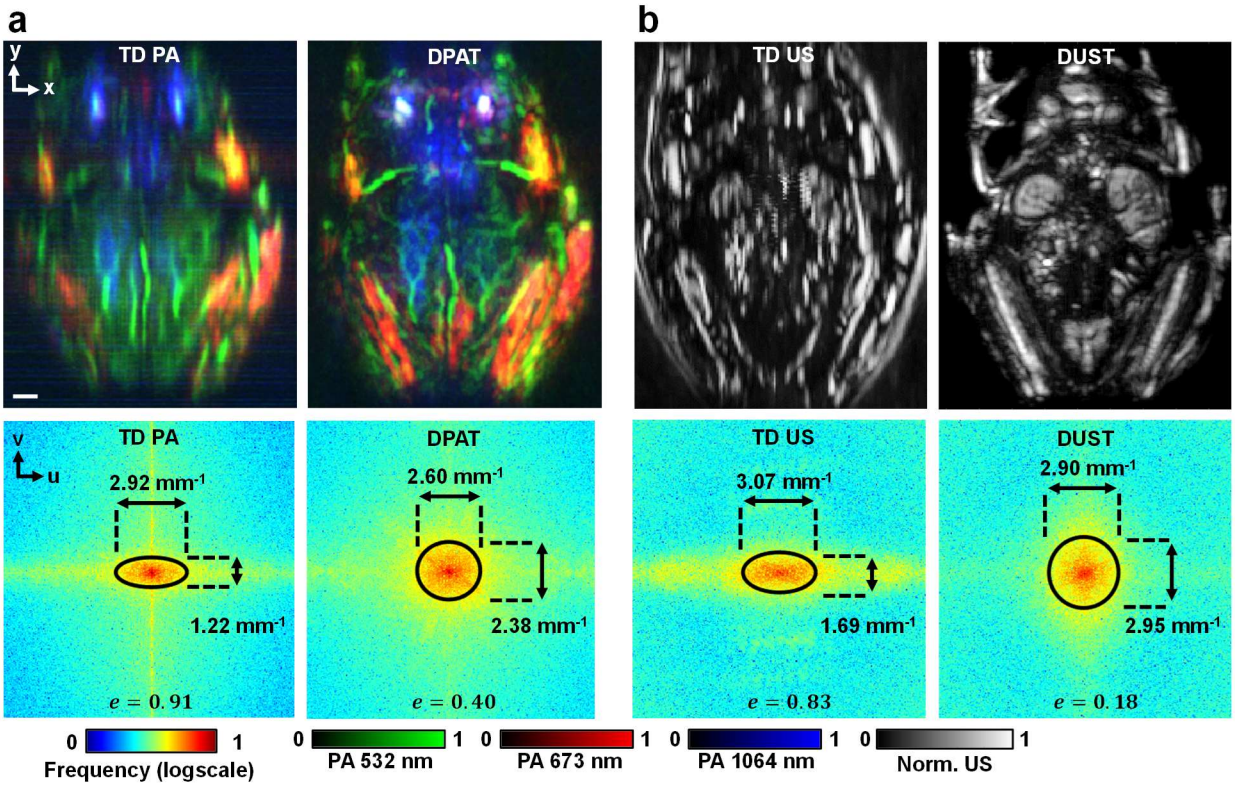

Supplementary Figure 17. Comparison of the spatial frequency spectrum in traditional PA/US imaging and 3D-DAT. (a) Traditional PA and DPAT images of a glassfrog (top row) and the corresponding spatial frequency spectrum images (bottom row). An ellipse was fit to the spatial frequency spectrum, and the FWHM was quantified along the long and short axes crossing the origin. A reduction in the eccentricity of the ellipse in DPAT compared to traditional PA is due to the improved elevational resolution. **(b)** Corresponding traditional US and DUST images of the same glassfrog. The spatial frequency spectrum of the DUST image similarly shows a lower eccentricity as a result of the improved elevational resolution, when compared to the traditional US image. Scale bar 2 mm.

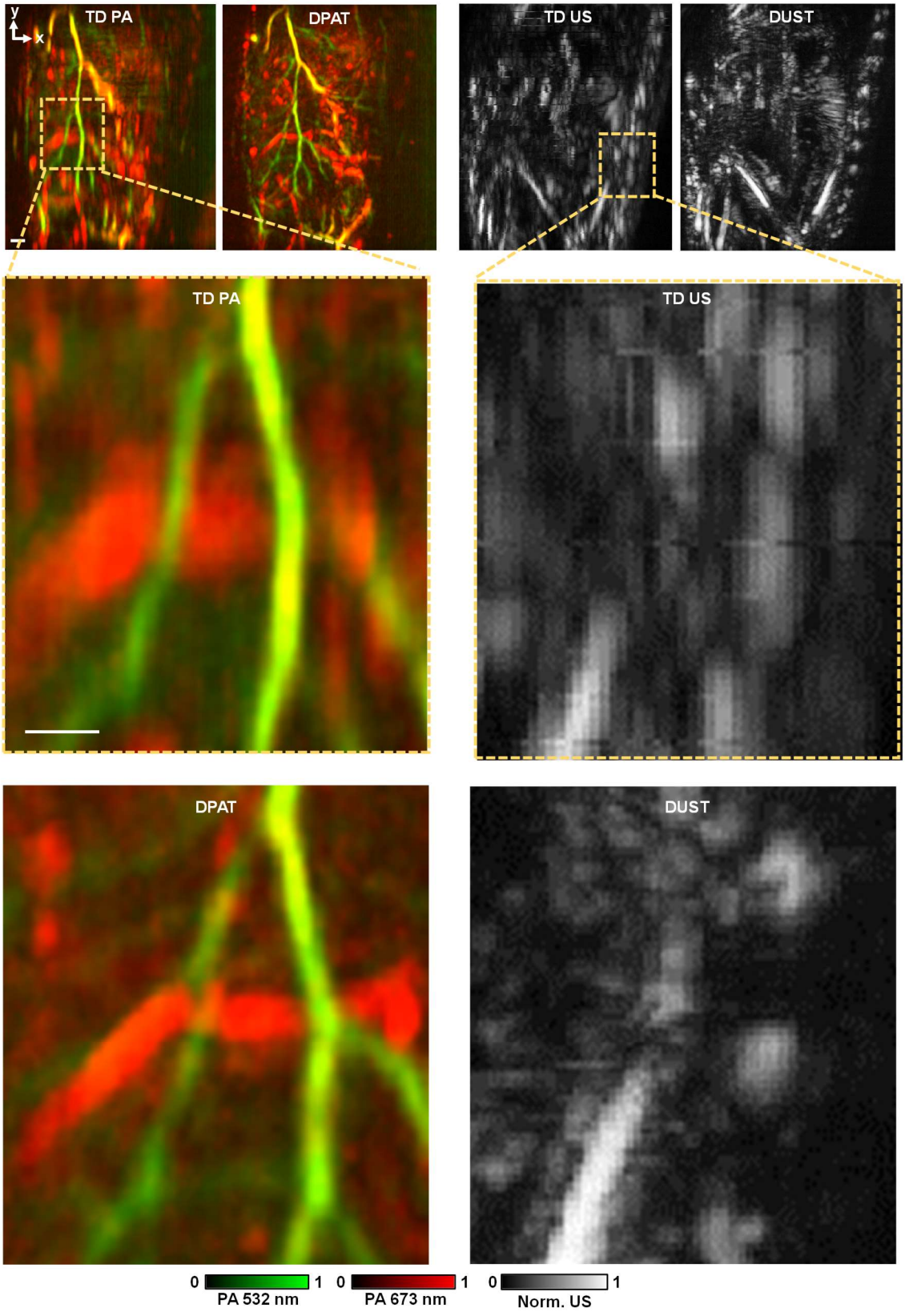
y
x
TD PA
DPAT
TD US
DUST
TD PA
TD US
DPAT
DUST
0
1
PA 532 nm
0
1
PA 673 nm
0
1
Norm. US

Supplementary Figure 18. 3D-DAT of a mouse *in-vivo.* DPAT shows a clear improvement in both resolution and sensitivity over traditional PA imaging in the close-up images of liver blood vessels. DUST similarly shows clear improvements compared to traditional US imaging in the close-up images of the vertebrae. Scale bars, 2 mm.

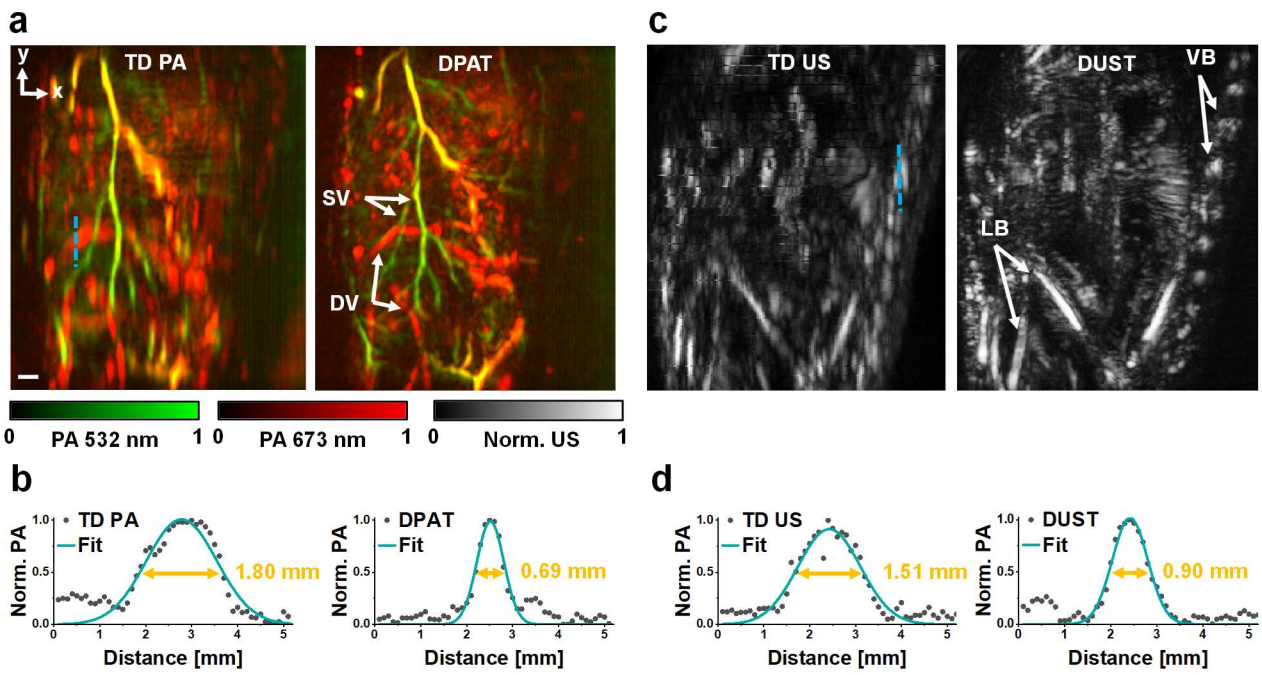

Supplementary Figure 19. Quantitative analysis of traditional PA/US imaging and 3D-DAT in a mouse *in vivo*. (a) Multispectral traditional PA and DPAT images of a mouse abdominal region. **(b)** Traditional PA (top) and DPAT (bottom) image profiles along the dashed blue line over a vessel shown in **(a)**. The FWHM of the image profile shows significantly improved resolution for DPAT. **(c)** Corresponding traditional US and DUST images of the mouse abdominal region. **(d)** Traditional US (top) and DUST (bottom) image profiles along the dashed blue line over a vertebra shown in **(c)**. The FWHM of the image profile similarly shows improved elevational resolution for DUST.

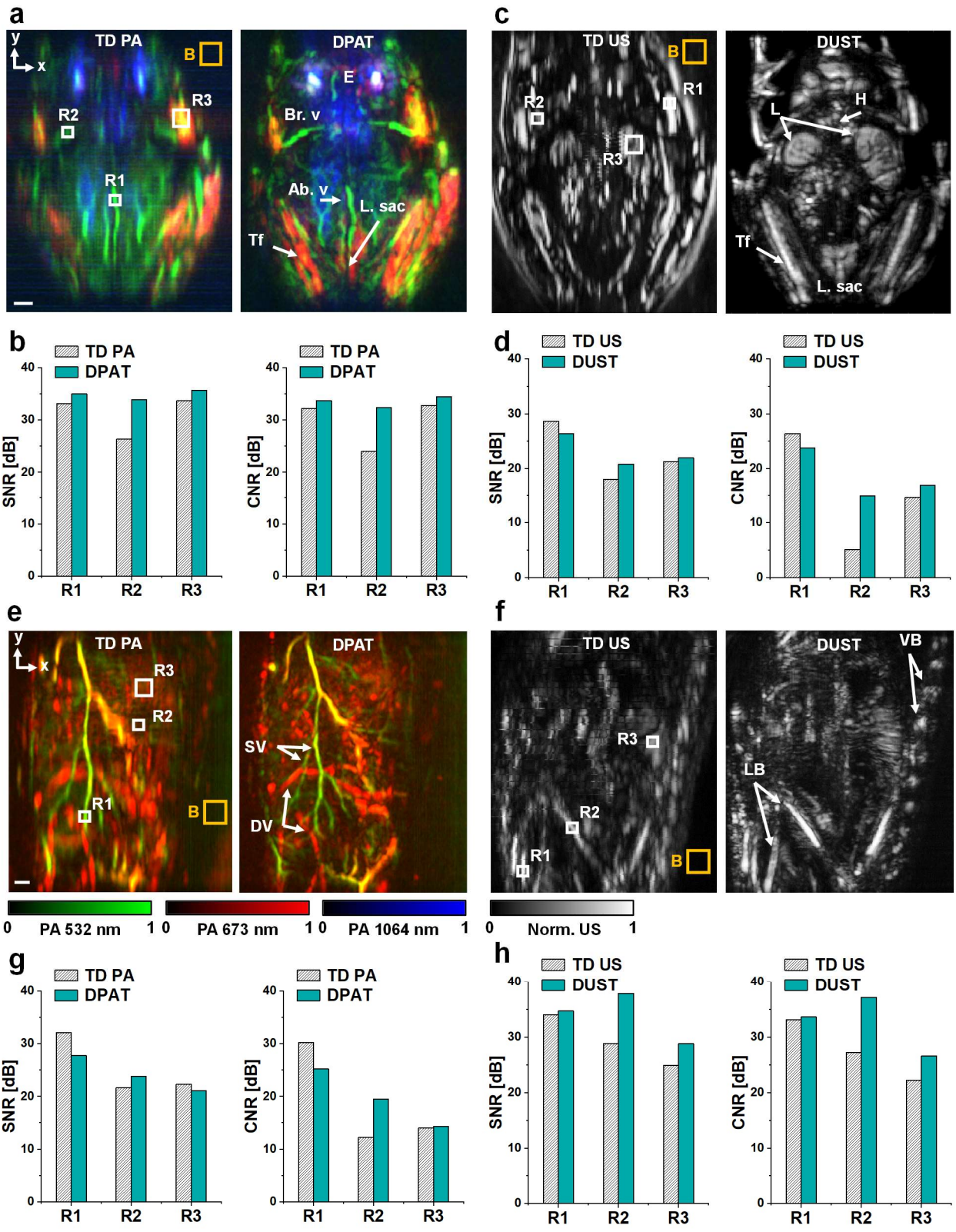
a
TD PA
DPAT
B
R1
R2
R3
E
Br. v
Ab. v
L. sac
Tf
c
TD US
DUST
L
H
b
TD PA
DPAT
SNR [dB]
CNR [dB]
d
TD US
DUST
e
SV
DV
f
LB
VB
PA 532 nm
PA 673 nm
PA 1064 nm
Norm. US
g
h

Supplementary Figure 20. *In-vivo* comparison of SNR and CNR between traditional PA/US imaging and 3D-DAT. (a) Traditional PA and DPAT images of a glassfrog. **(b)** SNR and CNR comparisons of three regions of interest (R) and background (B) shown in **(a)**. **(c)** Corresponding traditional US and DUST images of the glassfrog. **(d)** SNR and CNR comparisons of regions of interest (R) and background (B) shown in **(c)**. **(e)** Traditional PA and DPAT images of a mouse abdominal region. **(f)** Corresponding traditional US and DUST images of the mouse abdominal region. **(g)** SNR and CNR comparisons of regions of interest (R) and background (B) shown in **(e)**. **(h)** SNR and CNR comparisons of regions of interest (R) and background (B) shown in **(f)**.

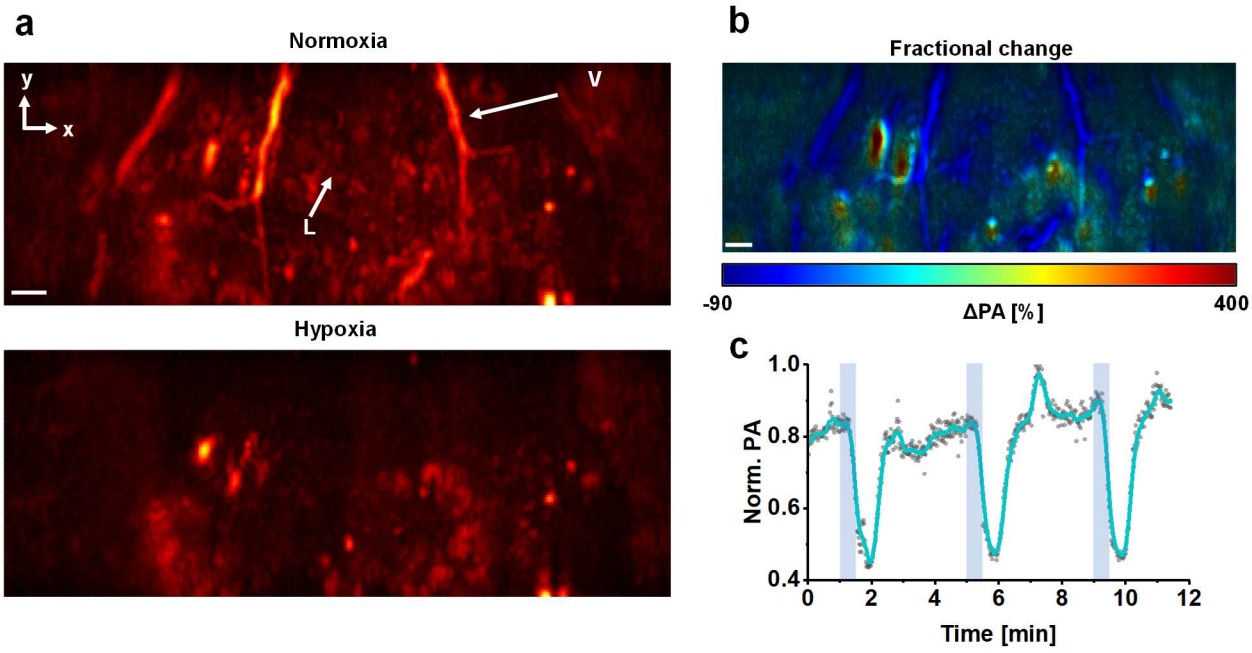

Supplementary Figure 21. Functional DPAT of hypoxia challenge in a mouse. (a) DPAT images of a mouse liver region at 1064 nm during normoxia and hypoxia conditions, showing the hypoxia-induced signal decrease. L, liver; V, vessel. **(b)** Fractional signal change of the mouse liver region from normoxia to hypoxia. The decrease in blood oxygenation of the two landmark blood vessels is clear. **(c)** The time course of the averaged PA signal intensity over three cycles of normoxia and hypoxia challenges. The aqua solid line is the moving-averaged data over a 20-points window of the gray raw data points. The shaded boxes indicate the duration of hypoxia challenges. Scale bars, 2 mm.

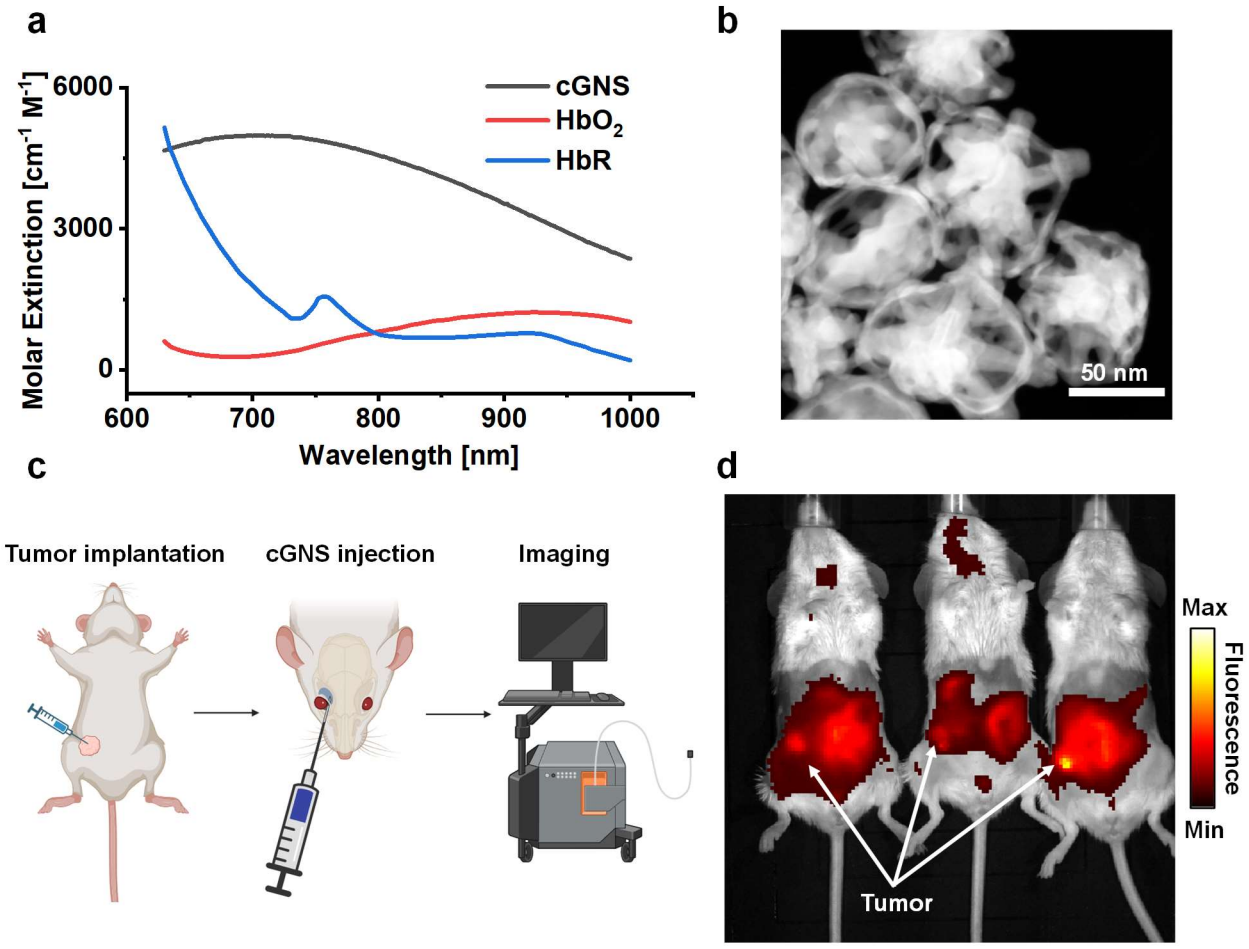

Supplementary Figure 22. Characterization of caged gold nanostars for a tumor model and fluorescence validation. (a) Molar extinction coefficient spectra of cGNS, oxyhemoglobin (HbO_2), and deoxyhemoglobin (HbR). DPAT images were acquired at 700 nm. **(b)** Transmission electron microscopy (TEM) images of the cGNS particles. **(c)** Experimental procedure for imaging cGNS on a tumor-bearing mouse. Created in BioRender. Menozzi, L. (2025) https://BioRender.com/s18n479. **(d)** IVIS fluorescence images of the tumor-bearing mice taken at 48 hours following cGNS injection (Excitation: 785 nm; Emission: 820 nm).

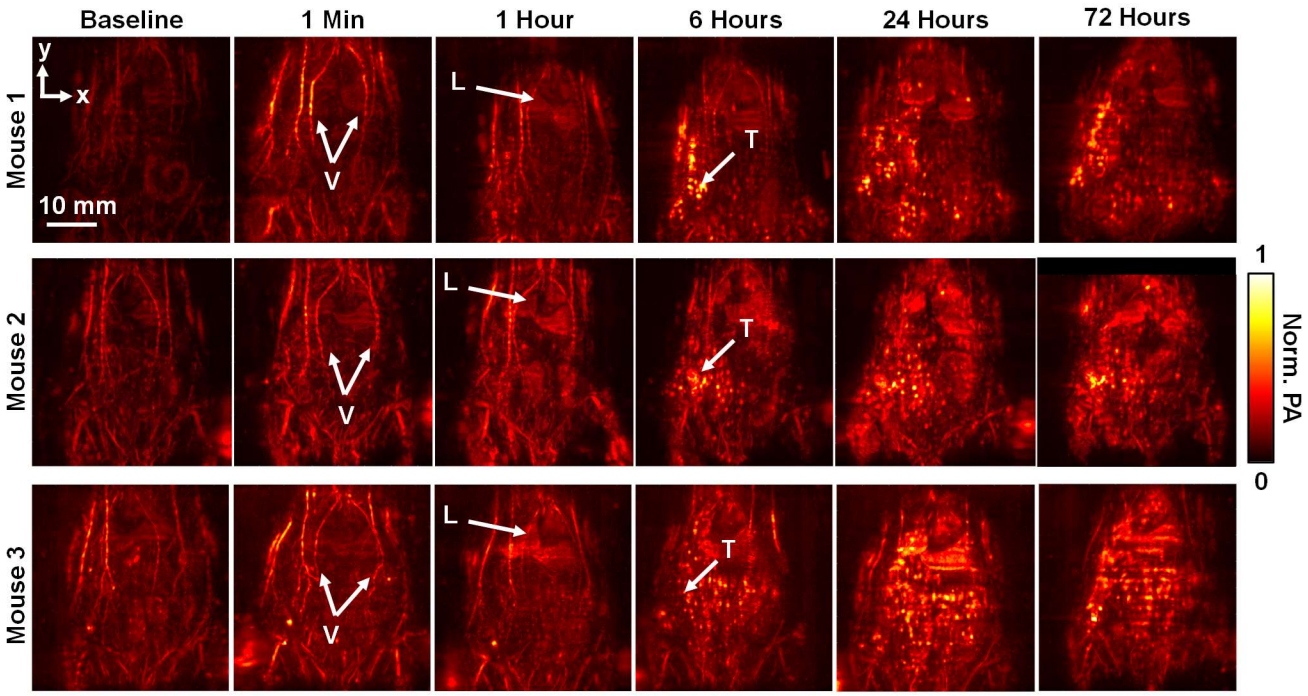

Supplementary Figure 23. DPAT of cGNS distribution on three tumor mice. Coronal maximum amplitude projections (MAPs) of the DPAT images acquired at 700 nm, from baseline (before cGNS injection) to 72 hours after the injection. Major blood vessels (V) became brighter right after the injection. The liver region (L) became more visible after 1 hour, and clear accumulation in the tumor region (T) was observed after 6 hours.

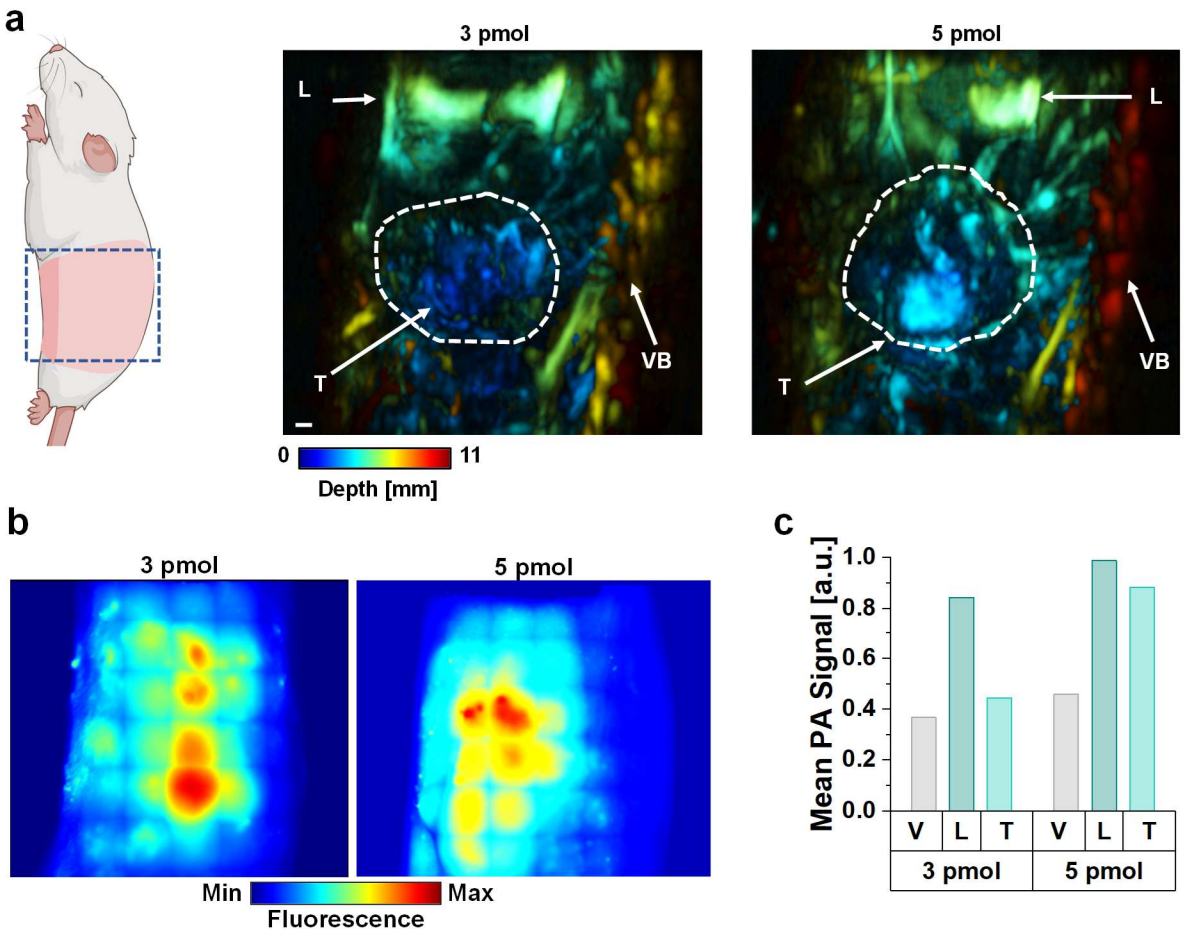

Supplementary Figure 24. DPAT images of cGNS-labeled tumor mice at various doses. (a) Depth-encoded DPAT images at 700 nm, 48 hours after injections of cGNS at two different doses of 3 pmol and 5 pmol. L, liver; T, tumor; VB, vertebrae. Created in BioRender. Menozzi, L. (2025) https://BioRender.com/o20i194. **(b)** Corresponding fluorescence images of the tumors. **(c)** Averaged PA signals in the vessel (V), liver (L), and tumor (T) regions.

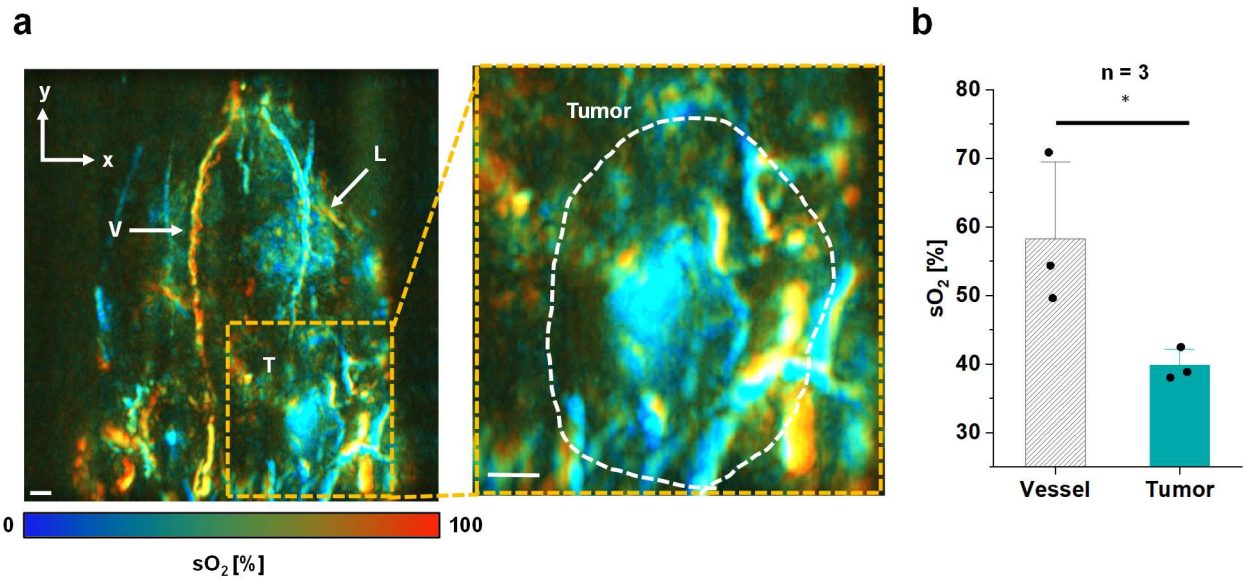

Supplementary Figure 25. Functional DPAT of mouse tumor. (**a**) DPAT images of blood oxygenation of a tumor-bearing mouse, with vessels (V), liver (L), and tumor (T) regions. A close-up image of the tumor region is also shown. (**b**) Comparison of averaged sO_2 levels in the tumor region and the skin vessels (n = 3). Scale bars, 2 mm.

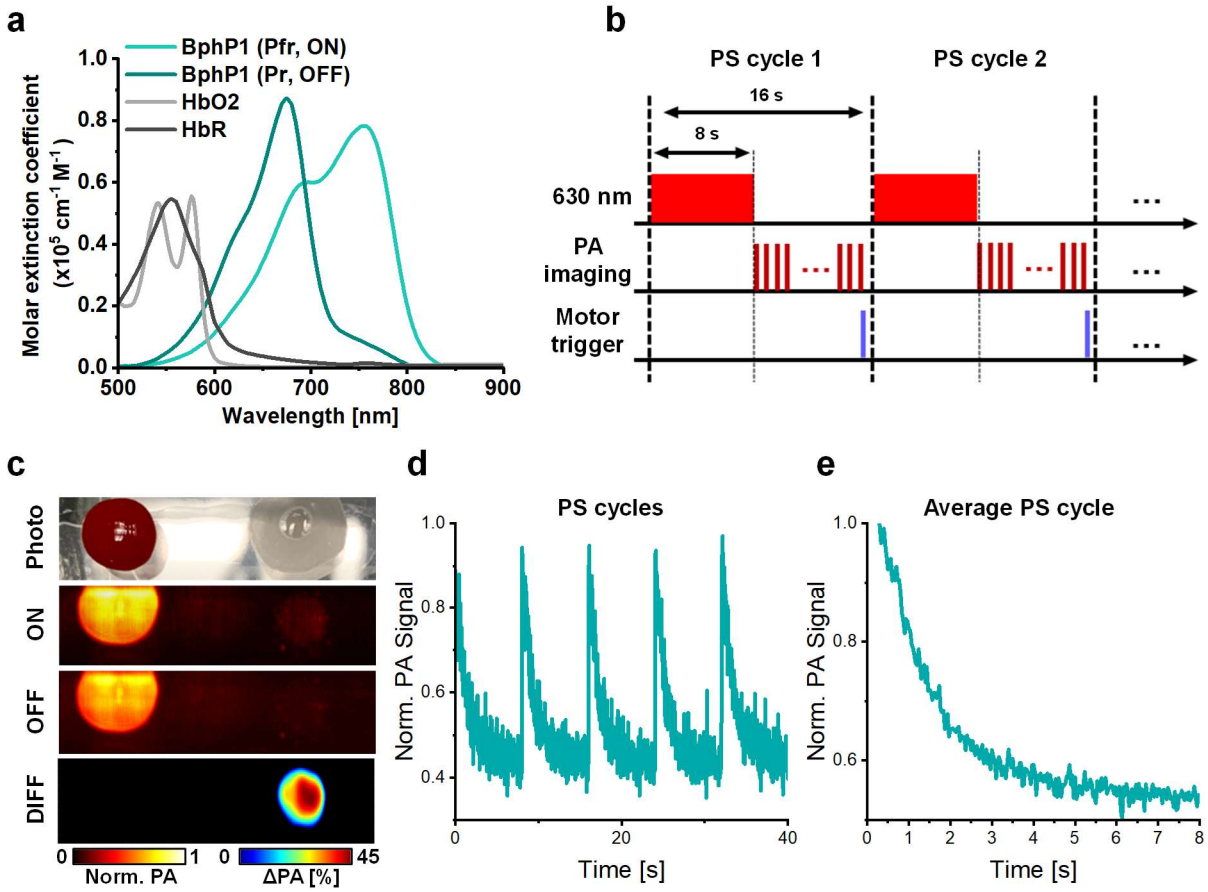

Supplementary Figure 26. PS-DPAT of BphP1-expressing tumor cells. (a) Optical extinction spectra of HbO_2, HbR, and BphP1 in both conformational states (Pr and Pfr). **(b)** Imaging sequence of PS-DPAT. A continuous wavelength (CW) laser at 630 nm is first used to convert BphP1 to the Pfr state (ON state). PS-DPAT at 750 nm then converts the protein back to the Pr state (OFF state). The linear-array transducer is stepped after every photoswitching cycle to generate a 3D volume. **(c)** Validation of PS-DPAT by imaging a drop of blood and a drop of BphP1-expressing tumor cells simultaneously. The BphP1-expressing tumor cells are extracted by taking the difference of the ON and OFF images and normalizing to the ON image. **(d)** Five representative photoswitching cycles of the PA signals at different elevational positions **(e)** The PA signals averaged over the five cycles in **(d)**.

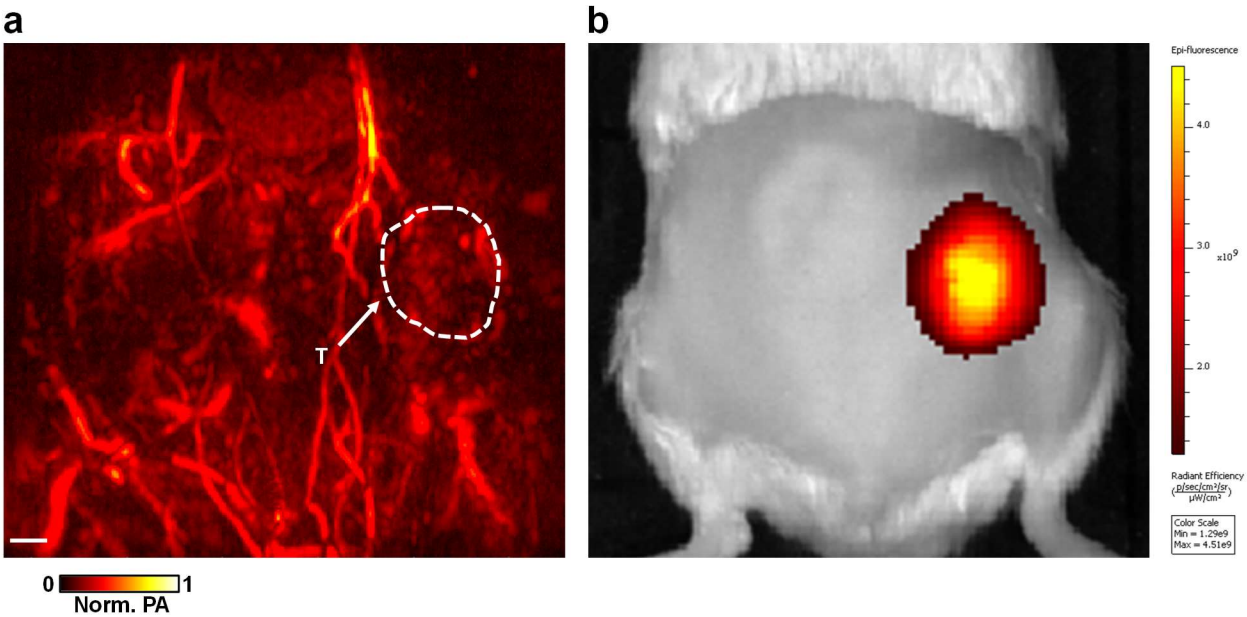

Supplementary Figure 27. PS-DPAT of a BphP1-expressing tumor mouse *in-vivo.* (**a**) DPAT image of a mouse bearing a BphP1-expressing tumor. (**b**) Corresponding IVIS fluorescence image of the mouse, showing the BphP1 fluorescence signals in the tumor. Scale bar, 2 mm.

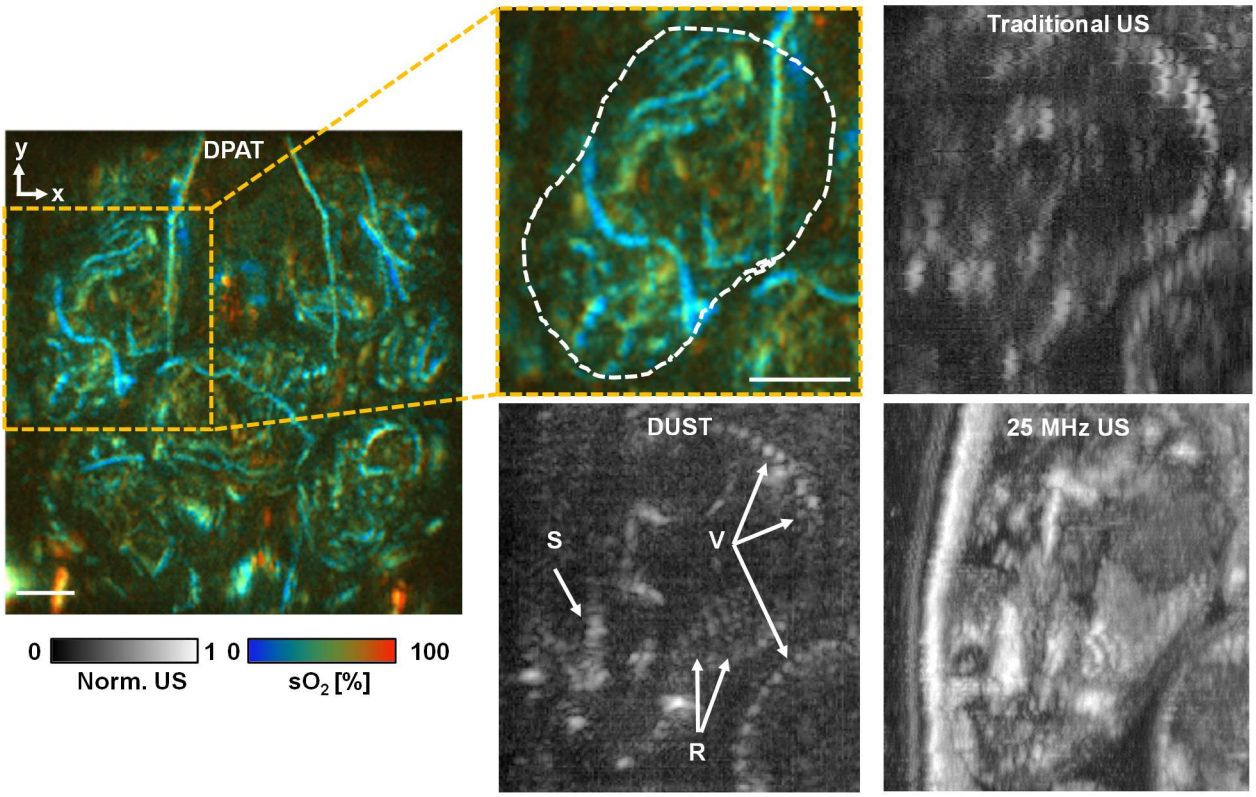

Supplementary Figure 28. 3D-DAT of a pregnant mouse. The DPAT image of the pregnant mouse at E18 is shown on the left, with a representative embryo marked by the dashed yellow box. In the DUST image of the same embryo, we can clearly distinguish the highly scattering structures, such as the skull (S), ribs (R), and vertebrae (V), which are not as clear in the traditional US image. The bottom right image shows the corresponding high-frequency ultrasound image acquired at 25 MHz. Scale bars, 5 mm.

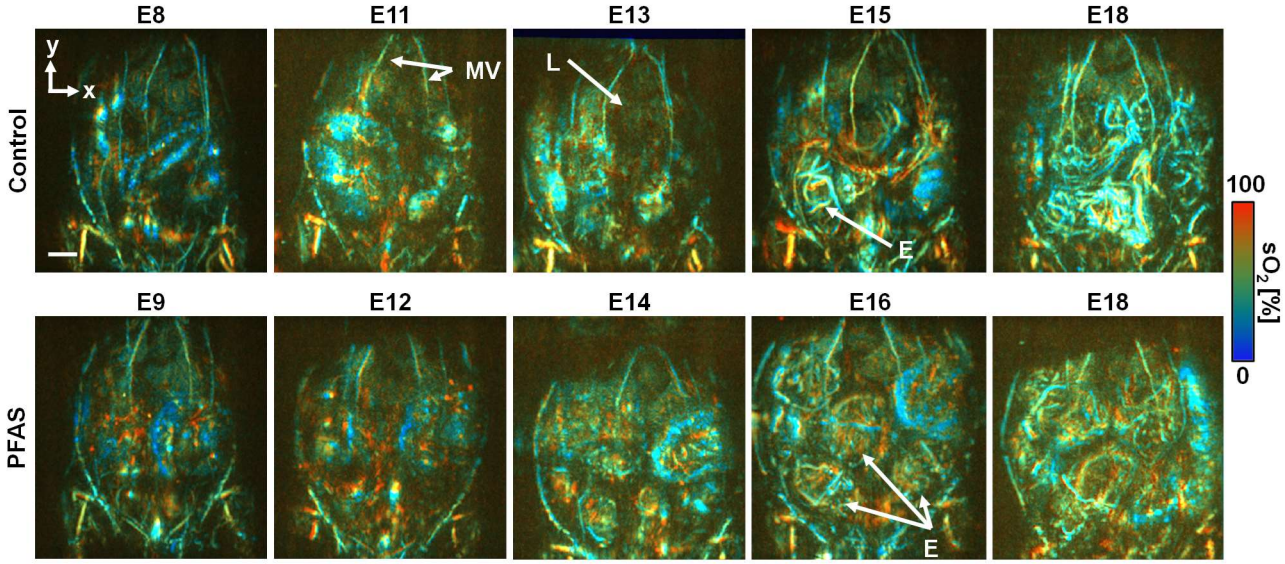

Supplementary Figure 29. Longitudinal DPAT of pregnant mice exposed to PFAS and the control group throughout the gestations. The PFAS-exposed embryos showed significantly higher oxygenation levels than the control group. E, embryo. L, liver. MV, maternal vessel. Scale bar, 5 mm.

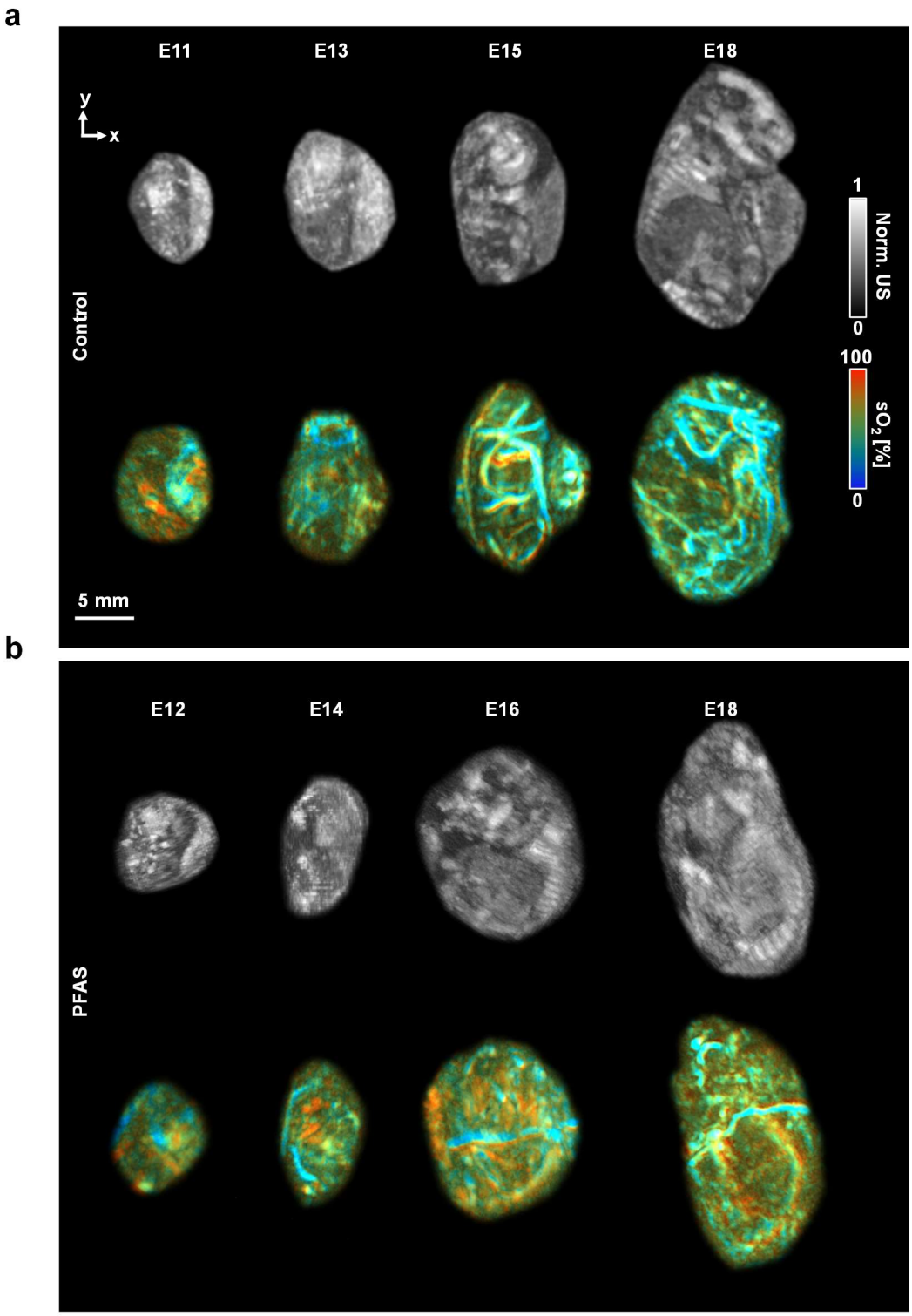

Supplementary Figure 30. The development of a single embryo in the PFAS-exposed mouse, imaged by DPAT and high-frequency US imaging. (a) Control mouse embryo development from E11 to E18. High-frequency US images are shown on

the top row and sO_2 images by DPAT are shown on the bottom row. **(b)** PFAS-exposed mouse embryo development from E12 to E18. Higher oxygenation levels can be observed throughout the development of the PFAS-exposed embryo when compared with the control embryo in **(a)**.

References

[1] R. S. Cobbold, *Foundations of biomedical ultrasound*. Oxford university press, 2006.

[2] J. L. Prince and J. M. Links, *Medical imaging signals and systems*. Pearson Prentice Hall Upper Saddle River, 2006.

[3] Y. Tang *et al.*, "High-fidelity Deep Functional Photoacoustic Tomography Enhanced by Virtual Point Sources," *Photoacoustics,* p. 100450, 2023.

[4] B. Seaton and B. B. Lloyd, "The effects of pH on the equilibrium constants of various models for the haemoglobin-oxygen equilibrium in vitro," *Respiration Physiology,* vol. 20, no. 2, pp. 209-230, 1974.

[5] B. Cox, J. Laufer, and P. Beard, "The challenges for quantitative photoacoustic imaging," in *Photons Plus Ultrasound: Imaging and Sensing 2009*, 2009, vol. 7177: SPIE, pp. 294-302.

[6] C. Taboada *et al.*, "Glassfrogs conceal blood in their liver to maintain transparency," *Science,* vol. 378, no. 6626, pp. 1315-1320, 2022.

[7] C. Taboada *et al.*, "Multiple origins of green coloration in frogs mediated by a novel biliverdin-binding serpin," *Proceedings of the National Academy of Sciences,* vol. 117, no. 31, pp. 18574-18581, 2020.